Novel coherent two-dimensional optical spectroscopy probes of chirality exchange and fluctuations in molecules

František Šanda[1,a)] and Shaul Mukamel[2,b)]
[1]*Institute of Physics, Faculty of Mathematics and Physics, Charles University, Ke Karlovu 5, Prague, 121 16, Czech Republic*
[2]*Department of Chemistry, University of California, Irvine, California 92697-2025, USA*

(Received 3 August 2011; accepted 16 October 2011; published online 16 November 2011)

We demonstrate how stochastic transitions between molecular configurations with opposite senses of chirality may be probed by 2D optical signals with specific pulse polarization configurations. The third-order optical response of molecular dimers (such as biphenyls) with dynamical axial chirality is calculated to order of k^2 in the wavevector of light. Spectroscopic signatures of equilibrium chirality fluctuations are predicted for three dynamical models (Ornstein-Uhlenbeck, two-state jump, and diffusion in double well) of the dihedral angle that controls the chirality. © *2011 American Institute of Physics*. [doi:10.1063/1.3658277]

I. INTRODUCTION

Virtually all biological molecules such as peptides, sugars, and nuclear bases are chiral. Chiral structures come in enantiomer pairs connected by a reflection symmetry (parity). Normally only one of them is biologically active.

Chirality can be either local and inherent to small molecular units or can arise from a chiral secondary or tertiary assembly of non-chiral units.[1] The most common origin of the former is a carbon atom substituted with four chemically different groups, α helices are the examples of chiral structures without stereogenic (chiral) centers. Molecules with inherent, axial, or planar chirality, have some stable geometry which is symmetric under reflection, but can fluctuate to assume chiral configurations. Alternatively the symmetric geometry can be unstable, and the enantiomers are two local minima of the free energy. Chirality then need not involve large amplitude motions of atoms (groups) within the molecule, and chirality exchange can be fast (picosecond).

While chiral enantiomers show large differences in their biological activity or chemical reactivity, most physical properties are identical, so that chirality can only be studied by a limited number of physical methods.[2–5] The simplest and most common is a linear spectroscopic technique–circular dichroism (CD): the difference between the absorption of left- and right-handed circularly polarized light.[6,7] Chirality of peptides is commonly investigated by vibrational circular dichroism in the infrared, or by Raman optical activity.[8,9] Electronic transitions of organometallic complexes, fullerenes, porphyrins, and chlorophylls have been studied in the visible regime.[10–13] The secondary and tertiary structure of proteins is often studied in the ultraviolet.[14,15] X-ray CD is used to characterize magnetic materials.[16,17] Equivalent information to CD may be obtained by looking at the $I_{yz} - I_{zy}$ tensor component of free induction decay for linearly polarized light propagating along x.[18]

Nonlinear optical measurements can monitor molecular processes on the femtosecond time scale.[19] The pump probe technique has been employed for monitoring time-dependent chirality of photoexcited molecules.[20] The secondary structure of peptides has been studied by coherent two-dimensional (2D) vibrational spectra.[21] Pulse shaping may be applied to better resolve signatures of chirality in 2D spectra.[22–24]

Microscopically, CD in isotropic ensembles (e.g., liquids) is related to $\vec{\mu} \cdot \vec{M}$, a pseudoscalar (changes sign under reflection), where $\vec{\mu}$ is the electric and $\vec{M}$ magnetic dipole. Chiral optical signals are generally weaker than their non-chiral counterparts. For CD, the ratio scales as $\propto kR \sim 10^{-3}$, where k is the optical wavevector and R is a typical molecular size ($kR \approx M/\mu$). Signals may be enhanced by tailored pulse polarization configurations.[25,26]

When the energy barrier between enantiomers is low, the exchange is fast, the enantiomers may not be isolated, and the CD signal vanishes. However, chirality exchange may be measured by probing two-time correlation function $\langle[\vec{\mu} \cdot \vec{M}](t)[\vec{\mu} \cdot \vec{M}](0)\rangle$.

In this paper we develop spectroscopic signatures of rapid equilibrium exchange of optical enantiomers. We focus on optical activity switching in dimers with axial chirality which contain no chiral center, but are arranged in a chiral geometry. Our model consists of two chemically identical groups bonded chemically along the x axis. The planar geometry ($\varphi = 0$) is achiral (symmetric to reflection by the yz plane). Distortion from planarity described by the angle φ gives rise to chirality, as shown in Fig. 1.

We consider three stochastic models of the coordinate dynamics $\varphi(t)$, which switches between the two senses of chirality (see Fig. 2). The first (i) has a potential minimum in the planar geometry ($\varphi = 0$), but the potential permits large chiral non-equilibrium fluctuations around the stable conformation. Model (ii) has a potential barrier at $\varphi = 0$ between two sharp minima of chiral conformations at $\pm\varphi_0$. Two-state jump dynamics then describes the chiral exchange between two stable conformations at mirror images $\pm\varphi_0$. In

a)Electronic mail: sanda@karlov.mff.cuni.cz.
b)Electronic mail: smukamel@uci.edu.

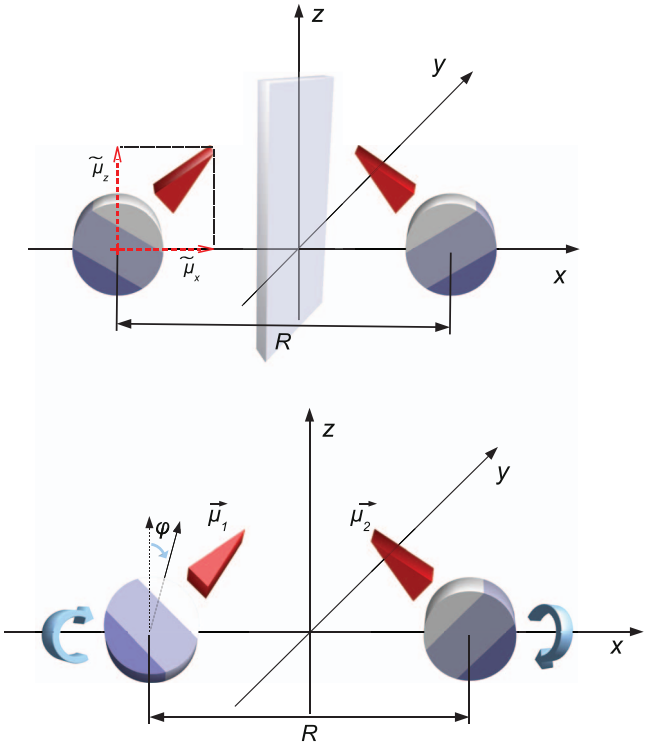

FIG. 1. Dimer geometry. Top: For $\varphi = 0$, the dimer is in xz plane, and is symmetric under the reflection through yz plane. Left chromophore corresponds to $\vec{\mu}_1|_{\varphi=0} = (\tilde{\mu}_x, 0, \tilde{\mu}_z)$, $\vec{M}_1, \ldots$, right chromophore corresponds to $\vec{\mu}_2|_{\varphi=0} = (-\tilde{\mu}_x, 0, \tilde{\mu}_z)$, $\vec{M}_2, \ldots$. Bottom: Axial chirality induced by twisting the groups by angle 2φ along x axis. The variation of multipoles with φ are given by Eq. (1) and in Appendix B.

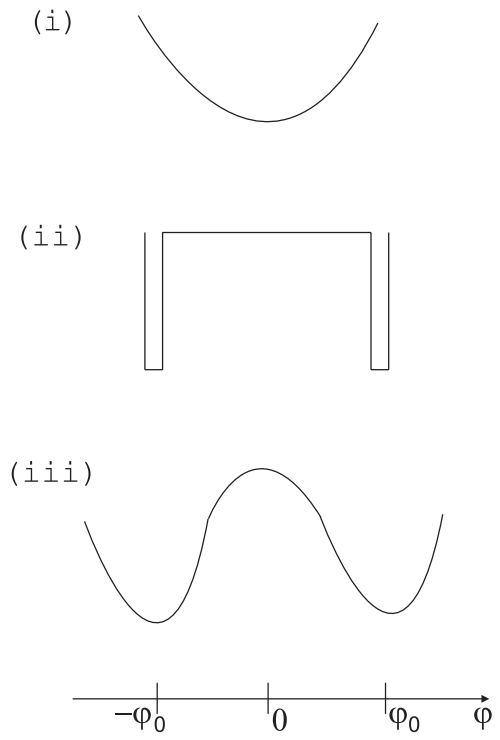

FIG. 2. Free energy profiles for the three models of diffusive (stochastic) dynamics of φ. Details are given in Appendix A.

model (iii), the potential around the stable conformations is soft and φ can vary continuously between two wells with minima at $\pm\varphi_0$ separated by a barrier at $\varphi = 0$. Details and parameterization of these models are given in Appendix A.

We will demonstrate how the rapid exchange of enantiomers may be monitored by third-order 2D optical spectroscopy and propose two pulse configurations that can accomplish this goal. We design a 2D photon echo signal $\propto (kR)^2$ that reveals the chirality exchange by looking at the two-time correlation function of $\vec{\mu} \cdot \vec{M}$, and may thus be used to monitor dynamics of $\varphi(t)$. Since $\propto (kR)^2$ signals are relatively weak, and hard to detect, we further discuss whether the dynamics of $\varphi(t)$ can be monitored without relying on the pseudoscalar $\vec{\mu} \cdot \vec{M}$. For instance, one of the dimer electronic eigenstates can carry no oscillator strength in the non-chiral geometry, but may acquire it in chiral configurations. Similar considerations will be used to propose a second pulse configuration, which contains signatures of chirality exchange even to order $\propto (kR)^0$.

II. THE CHIRAL DIMER MODEL

For the model of Fig. 1 in the non-chiral (planar) geometry the electric transition dipole moment of both groups lies in the xz plane $\vec{\mu}_1|_{\varphi=0} = (\tilde{\mu}_x, 0, \tilde{\mu}_z)$ and $\vec{\mu}_2|_{\varphi=0} = (-\tilde{\mu}_x, 0, \tilde{\mu}_z)$. The geometry becomes chiral when the planar geometry is distorted by angle 2φ around the x axis. The transition dipoles of the two chromophores are then given by

$$\begin{aligned} \vec{\mu}_1 &= (\tilde{\mu}_x, \tilde{\mu}_z \sin\varphi, \tilde{\mu}_z \cos\varphi) \\ \vec{\mu}_2 &= (-\tilde{\mu}_x, -\tilde{\mu}_z \sin\varphi, \tilde{\mu}_z \cos\varphi). \end{aligned} \tag{1}$$

Expressions for the other low multipoles of the two groups, magnetic dipoles $\vec{M}_i$, and electric quadrupoles $\overleftrightarrow{Q}_i$ are given in Appendix B.

Each chromophore will be modeled as a two electronic level system (with levels e_i, g_i) described by the exciton operators $B_i^\dagger \equiv |e_i\rangle\langle g_i|$ and the dimer is described by the Frenkel exciton Hamiltonian (we set $\hbar = 1$) (Ref. 27),

$$H = \varepsilon B_1^\dagger B_1 + \varepsilon B_2^\dagger B_2 + J(B_2^\dagger B_1 + B_1^\dagger B_2), \tag{2}$$

where

$$\begin{aligned} J(\varphi) &= \left\{ \frac{\vec{\mu}_1 \cdot \vec{\mu}_2}{R^3} - 3\frac{(\vec{\mu}_1 \cdot \vec{R})(\vec{\mu}_2 \cdot \vec{R})}{R^3} \right\} \\ &= \frac{\tilde{\mu}_z^2 \cos(2\varphi)}{R^3} + \frac{2\tilde{\mu}_x^2}{R^3} \end{aligned} \tag{3}$$

is the (electric) dipole-dipole coupling, and $\vec{R} = (R, 0, 0)$ is the distance between the two chromophores. We shall neglect dipole-quadrupole and quadrupole-quadrupole, etc. couplings.

The Hamiltonian (Eq. (2)) can be diagonalized by introducing the symmetric $B_+^\dagger = \frac{1}{\sqrt{2}}(B_1^\dagger + B_2^\dagger)$ and antisymmetric $B_-^\dagger = \frac{1}{\sqrt{2}}(B_1^\dagger - B_2^\dagger)$ exciton creation operators to yield

$$H = (\varepsilon + J)B_+^\dagger B_+ + (\varepsilon - J)B_-^\dagger B_- .$$

We shall calculate the nonlinear optical response of the dimer to sequences of short laser pulses. For calculating the chiral optical response we keep all $\sim \vec{k}\cdot\vec{r}$ (to first order in the wavevector of light $\vec{k}$) terms in the multipole expansion of the matter-field Hamiltonian, i.e. the electric dipole, magnetic dipole, and electric quadrupole. The matter-field interaction in the rotating wave approximation and in the local basis is

$$H_{\rm int} = -\sum_{\alpha=x,y,z}\sum_{j=1,2} E_\alpha(t) e^{i(-1)^j \vec{k}\cdot\vec{R}/2} B_j^\dagger \Big\{ \mu_{j,\alpha} + i\sum_{\beta=x,y,z} k_\beta Q_{j,\alpha\beta} - \sum_{\beta,\gamma=x,y,z} \epsilon_{\alpha\beta\gamma} \mathsf{k}_\beta M_{j,\gamma} \Big\} + h.c, \tag{4}$$

where $\vec{E}(t)$ is the electric field of the laser pulses at the origin of molecular frame and $\vec{\mathsf{k}} \equiv \vec{k}/k$ is the unit vector of $\vec{k}$.

We next expand Eq. (4) in multipoles using the exciton $B_\pm^\dagger$ basis and Taylor series $e^{i\vec{k}\cdot\vec{R}/2} = 1 + i\vec{k}\cdot\vec{R}/2 + \mathcal{O}(k^2)$. The local electric dipoles,

$$\begin{aligned}&\vec{\mu}_1 B_1^\dagger e^{-i\vec{k}\cdot\vec{R}/2} + \vec{\mu}_2 B_2^\dagger e^{i\vec{k}\cdot\vec{R}/2} \\ &= (\vec{\mu}_+ + i\vec{k}\cdot\overleftrightarrow{Q}_{1\leftrightarrow 2,+} - \vec{\mathsf{k}}\times\vec{M}_{1\leftrightarrow 2,+}) B_+^\dagger \\ &\quad + (\vec{\mu}_- + i\vec{k}\cdot\overleftrightarrow{Q}_{1\leftrightarrow 2,-} - \vec{\mathsf{k}}\times\vec{M}_{1\leftrightarrow 2,-}) B_-^\dagger + \mathcal{O}(k^2),\end{aligned} \tag{5}$$

contribute to all global multipoles of the dimer. In Eq. (5), the transition dipole moments are

$$\vec{\mu}_+ = \frac{1}{\sqrt{2}}(\vec{\mu}_1 + \vec{\mu}_2) = \sqrt{2}(0, 0, \tilde{\mu}_z \cos\varphi),$$
$$\vec{\mu}_- = \frac{1}{\sqrt{2}}(\vec{\mu}_1 - \vec{\mu}_2) = \sqrt{2}(\tilde{\mu}_x, \tilde{\mu}_z \sin\varphi, 0).$$

The dipole moment μ_+ has a single vector component. Therefore, it can be taken real $\vec{\mu}_+(\varphi) = \vec{\mu}_+^*(\varphi)$ in proper phase convention. The electric quadrupoles of Eq. (5) (symmetric part of the tensors $-\mu_{-,\alpha}R_\beta/2$ and $-\mu_{+,\alpha}R_\beta/2$) are

$$\overleftrightarrow{Q}_{1\leftrightarrow 2,+} = \frac{-1}{2\sqrt{2}}\begin{pmatrix} 2R\tilde{\mu}_x & R\tilde{\mu}_z\sin(\varphi) & 0 \\ R\tilde{\mu}_z\sin(\varphi) & 0 & 0 \\ 0 & 0 & 0\end{pmatrix},$$

$$\overleftrightarrow{Q}_{1\leftrightarrow 2,-} = \frac{-1}{2\sqrt{2}}\begin{pmatrix} 0 & 0 & R\tilde{\mu}_z\cos(\varphi) \\ 0 & 0 & 0 \\ R\tilde{\mu}_z\cos(\varphi) & 0 & 0\end{pmatrix}. \tag{6}$$

Finally, the magnetic dipoles (antisymmetric part) are given by

$$\vec{M}_{1\leftrightarrow 2,+} = \frac{-i}{2\sqrt{2}}(0, 0, kR\tilde{\mu}_z \sin\varphi),$$
$$\vec{M}_{1\leftrightarrow 2,-} = \frac{i}{2\sqrt{2}}(0, kR\tilde{\mu}_z \cos\varphi, 0). \tag{7}$$

The total multipoles are obtained by adding the local magnetic dipoles and electric quadrupoles, $\vec{M}_+ \equiv \frac{1}{\sqrt{2}}[\vec{M}_1 + \vec{M}_2] + \vec{M}_{1\leftrightarrow 2,+}$, and $\overleftrightarrow{Q}_+ \equiv \frac{1}{\sqrt{2}}[\overleftrightarrow{Q}_1 + \overleftrightarrow{Q}_2] + \overleftrightarrow{Q}_{1\leftrightarrow 2,+}$ (see Appendix B for details).[28] Contributions given by Eqs. (6) and (7), however, typically dominate $\overleftrightarrow{Q} \approx \overleftrightarrow{Q}_{1\leftrightarrow 2}$, $\vec{M} \approx \vec{M}_{1\leftrightarrow 2}$.[29]

The interaction Hamiltonian in the $B_+^\dagger$, $B_-^\dagger$ basis is finally given by

$$H_{\rm int} = -\sum_{\alpha=x,y,z}\sum_{j=+,-} E_\alpha B_j^\dagger \Big\{ \mu_{j,\alpha} + i\sum_{\beta=x,y,z} k_\beta Q_{j,\alpha\beta} - \sum_{\beta,\gamma=x,y,z} \epsilon_{\alpha\beta\gamma}\mathsf{k}_\beta M_{j,\gamma}\Big\} + h.c. \tag{8}$$

III. THE CHIRAL LINEAR RESPONSE

We will assume that symmetric and antisymmetric levels can be probed separately. The field-matter interaction Hamiltonian (repeated Greek indices are summed over) is then

$$H_{\rm int} = -E_\alpha(t)\mathcal{J}_\alpha(t)B^\dagger + h.c., \tag{9}$$

where $B^\dagger$ can be either $B_+^\dagger$, or $B_-^\dagger$. The first order (in k) of the multipole expansion

$$\mathcal{J}_\alpha = \mu_\alpha + k_\beta T_{\alpha\beta} + k_\beta k_\gamma Y_{\alpha\beta\gamma} + \ldots, \tag{10}$$

will be sufficient for our discussion. Equations (9) and (10) are abstract forms of the expansion of Eq. (8). Note, that the electric quadrupole $\overleftrightarrow{Q}$ is the symmetric and magnetic dipole $\vec{M}$ is the antisymmetric part of tensor $\overleftrightarrow{T}$,

$$T_{\alpha\beta} = i\,Q_{\alpha\beta} - \epsilon_{\alpha\beta\gamma}M_\gamma/k.$$

So far we used the molecular frame introduced in Fig. 1. To compare with experiment we must average over molecular orientations in space. In isotropic ensembles, molecular and lab frame averages of tensors are connected by simple rules described in Ref. 30. We will use variables with overbar $\bar{\mu}, \bar{\mathcal{J}}, \bar{T}, \ldots$ to denote laboratory frame variables compared to $\mu, \mathcal{J}$ in the molecular frame.

In addition we must average over the stochastic paths of the chiral angle $\varphi(t)$. The summation $\langle\ldots\rangle_\varphi \equiv \int \ldots G(t)P[\varphi(t)]\mathcal{D}[\varphi(t)]$ includes the accumulated phase $G(t)$. For the linear response $G(t) = e^{-i\varepsilon-\Gamma t}e^{\mp i\int_0^t J(\varphi(t'))dt'}$, where the upper (lower) sign holds for symmetric (antisymmetric) exciton. Γ is the dephasing rate, $P[\varphi(t)]$ is the probability density for path $\varphi(t)$ and $\int\mathcal{D}[\varphi(t)]$ stands for path integration. Hereafter, $\langle\ldots\rangle$ will denote the total (both orientational and $\langle\ldots\rangle_\varphi$) averaging.

The absorption spectrum is given by the correlation function of $\mathcal{J}$

$$I_{\alpha\beta}(\omega) = \int_0^\infty I_{\alpha\beta}(t)e^{i\omega t}dt, \tag{11}$$

$$I_{\alpha\beta}(t) = \langle\bar{\mathcal{J}}_\alpha^*(t)\bar{\mathcal{J}}_\beta(0)\rangle. \tag{12}$$

Expanding Eq. (12) by using Eq. (10), we get

$$I_{\alpha\beta}(t) = \langle\bar{\mu}_\alpha^*(t)\bar{\mu}_\beta(0)\rangle + k_\gamma\langle\bar{T}_{\alpha\gamma}^*(t)\bar{\mu}_\beta(0)\rangle + k_\gamma\langle\bar{\mu}_\alpha^*(t)\bar{T}_{\beta\gamma}(0)\rangle + \mathcal{O}(k^2). \tag{13}$$

Orientational averaging is carried out by using the rules of Ref. 30,

$$\langle \bar{\mu}^*_\alpha(t)\bar{\mu}_\beta(0)\rangle = \frac{1}{3}\delta_{\alpha\beta}\langle \mu^*_\gamma(t)\mu_\gamma(0)\rangle_\varphi,$$

$$\langle \bar{T}^*_{\alpha\gamma}(t)\bar{\mu}_\beta(0)\rangle = \frac{1}{3k}\epsilon_{\alpha\beta\gamma}\langle M^*_\delta(t)\mu_\delta(0)\rangle_\varphi,$$

$$\langle \bar{\mu}^*_\alpha(t)\bar{T}_{\beta\gamma}(0)\rangle = \frac{1}{3k}\epsilon_{\alpha\gamma\beta}\langle \mu^*_\delta(t)M_\delta(0)\rangle_\varphi.$$

The electric quadrupole contributions vanish upon orientation averaging in isotropic ensembles $\langle \bar{Q}^*_{\alpha\gamma}(t)\bar{\mu}_\beta(0)\rangle = \frac{1}{6}\epsilon_{\alpha\beta\gamma}\epsilon_{\alpha'\beta'\gamma'}\langle Q^*_{\alpha'\beta'}(t)\mu_{\gamma'}(0)\rangle = 0$.

Each term in Eq. (13) has distinct tensor structure,

$$I_{\alpha\beta}(t) = \frac{1}{3}\delta_{\alpha\beta}\langle \mu^*_\gamma(t)\mu_\gamma(0)\rangle_\varphi + \frac{1}{3}\epsilon_{\alpha\beta\gamma}\mathsf{k}_\gamma\left[\langle M^*_\delta(t)\mu_\delta(0)\rangle_\varphi - \langle \mu^*_\delta(t)M_\delta(0)\rangle_\varphi\right].$$

Only the second component $\propto\epsilon_{\alpha\beta\gamma}$ is chiral. Assuming that light propagates along x $\vec{k} = (k, 0, 0)$, the chiral absorption signal is given by $I_{yz}(t)$, or $I_{zy}(t)$.

Applying these results to our model system and using the Onsager reciprocity relation,[31] we get for the chiral signal,

$$I_{yz}(t) = -I_{zy}(t) = i\frac{2}{3}\int \mathrm{Im}[M^*_\delta(t)\mu_\delta(0)] \times e^{-\Gamma t}e^{-i\int_0^t(\varepsilon\pm J(t'))dt'}P[\varphi(t)]\mathcal{D}[\varphi(t)]. \quad (14)$$

Equation (14) vanishes in racemic mixtures whose dynamics is invariant to reflection $\varphi\to-\varphi$ (i.e., $P[\varphi(t)] = P[-\varphi(t)]$) since $M^*_\delta(t)\mu_\delta(0)$ is odd in φ and the coupling $J(\varphi)$ is even. Linear signals thus may not be used for probing chirality exchange.

In order to interpret the nonlinear spectra calculated below, we first examine the CD signal of molecules with fixed φ. To that end we formally rewrite Eq. (14) assuming slow φ dynamics $\varphi(t) = \varphi(0)$ (i.e., changes slowly on the $1/J$ time scale, see Eq. (C1)). In the $\vec{M}_{1\leftrightarrow 2} \gg \vec{M}_i$ limit, we get

$$I_{yz}(t) \approx \pm i\frac{kR}{6}|\tilde{\mu}_z|^2 e^{-\Gamma t}\int \sin(2\varphi)e^{-i[\varepsilon\pm J(\varphi)]t}\rho^{\mathrm{eq}}(\varphi)d\varphi, \quad (15)$$

where ρ^{eq} is the equilibrium density of φ (Eqs. (A4) and (A9)). We next decompose the spectrum (Eq. (11)) into the contributions $I(\omega, \varphi)$ from dimers with a given angle φ, and write $I(\omega) = \int \mathcal{I}(\omega, \varphi)d\varphi$, where

$$\mathcal{I}_{yz}(\omega, \varphi) \approx \frac{kR}{6}|\tilde{\mu}_z|^2\frac{\pm i}{\Gamma - i[\omega - (\varepsilon \pm J(\varphi))]}\sin(2\varphi)\rho^{\mathrm{eq}}(\varphi). \quad (16)$$

The real and the imaginary parts of $\mathcal{I}_{zy}(\omega, \varphi)$ are shown in Fig. 3 for the $B^\dagger_+$ exciton of a molecular dimer with harmonic (model (i)) and the double well (model (iii)) potentials of φ described in Appendix A. To simplify the parameterization we denoted $J_\Delta \equiv J(0) - J(\pi/4)$, and $\varepsilon_s \equiv \varepsilon + J(\pi/4)$; most spectral features of the symmetric state are then contained within an interval of $\omega \in (\varepsilon_s - J_\Delta, \varepsilon_s + J_\Delta)$. The spectrum is odd with respect to φ, and is localized along the curve $\omega \sim \varepsilon + J(\varphi)$, which closely follows the $\cos(2\varphi)$ form of the coupling (Eq. (3)). Along this curve the real part abruptly switches its sign, while the imaginary part is peaked. Integration of odd function $\mathcal{I}_{zy}$ over φ yields a vanishing total CD signal, but it will prove useful for interpreting higher signals to integrate the absolute values instead. The integrated real part, $\mathrm{Re}\,Y(\omega) \equiv \int|\mathrm{Re}\,\mathcal{I}_{yz}(\omega, \varphi)|d\varphi$, and imaginary part, $\mathrm{Im}\,Y(\omega) \equiv \int|\mathrm{Im}\,\mathcal{I}_{yz}(\omega, \varphi)|d\varphi$, are plotted in Fig. 4 along with the absorption line shape $\mathrm{Re}\,I_{xx}(\omega) = \int\cos^2\varphi\Gamma(\Gamma^2 + \omega^2)^{-1}\rho^{\mathrm{eq}}(\varphi)d\varphi$. Peak positions and profiles show the combined effects of the equilibrium densities (Eq. (A4)) and the geometric factor $\sin(2\varphi)$ from Eq. (16). In particular, features of $\rho^{eq}(\varphi)$ are responsible for shift in the central peak frequency between the two models through Eq. (3), while the geometric factor causes slight shifts in the central peak frequencies from the absorption line shapes. This may allow to determine φ_0 and σ experimentally once we relate Fig. 4 to the 2D spectrum.

IV. THE THIRD-ORDER CHIRAL RESPONSE

The three-pulse photon echo signal is described by the third-order response function,[32]

$$\mathcal{R}_{\alpha\beta\gamma\delta} = \langle \bar{\mathcal{J}}^*_\alpha(\tau_3)\bar{\mathcal{J}}_\beta(\tau_2)\bar{\mathcal{J}}_\gamma(\tau_1)\bar{\mathcal{J}}^*_\delta(0)\rangle. \quad (17)$$

Here, 0, τ_1, and τ_2 are the arrival times of the three pulses, and τ_3 is the time when the response is monitored. Hereafter, we change the time variables and use the intervals $t_1 = \tau_1$, $t_2 = \tau_2 - \tau_1$, and $t_3 = \tau_3 - \tau_2$.

The phase factors $G(t_3, t_2, t_1)$ for the averaging $\langle\ldots\rangle_\varphi = \int\ldots G(t_3, t_2, t_1)P[\varphi(t)]\mathcal{D}[\varphi(t)]$ now depend on the electronic density matrix during t_2. Decoherence takes place during the evolution of $|+\rangle\langle-|$. The resulting signal decay is indistinguishable from the decay of dipole correlations, which is the main effect of chirality dynamics we are looking for. We thus neglect possible coherences between $B^\dagger_+$ and $B^\dagger_-$ by assuming spectrally narrow pulses so that the first two pulses select the same level. We found that nonlinear signals do not show any clear signatures of chiral dynamics (neither in the magnitude nor in the shapes of cross peaks of 2D spectra) associated with varying frequency of the third pulse. We thus separately analyze the nonlinear response of the symmetric and antisymmetric levels assuming that they can be resolved.

These assumptions gives our final result for the phase factor,

$$G(t_3, t_2, t_1) = e^{-\Gamma(t_1+t_3)}e^{i\varepsilon(t_1-t_3)}e^{\pm i\int_0^{t_1}J(\varphi(t'))dt'\mp i\int_0^{t_3}J(\varphi(t_1+t_2+t'))dt'}.$$

$\langle\ldots\rangle_\varphi$ may be evaluated using the stochastic Liouville equations,[33,34] given in Appendix C.

A. Signatures of chirality exchange in the 2D spectrum of the symmetric exciton

Optical probes of chirality exchange are connected with the two-time correlation function of the pseudoscalar $\vec{\mu}\cdot\vec{M}$. These signals scale as $\propto(kR)^2$, so they are weak and can best be observed when the stronger $\propto(kR)^0$ and $\propto(kR)^1$

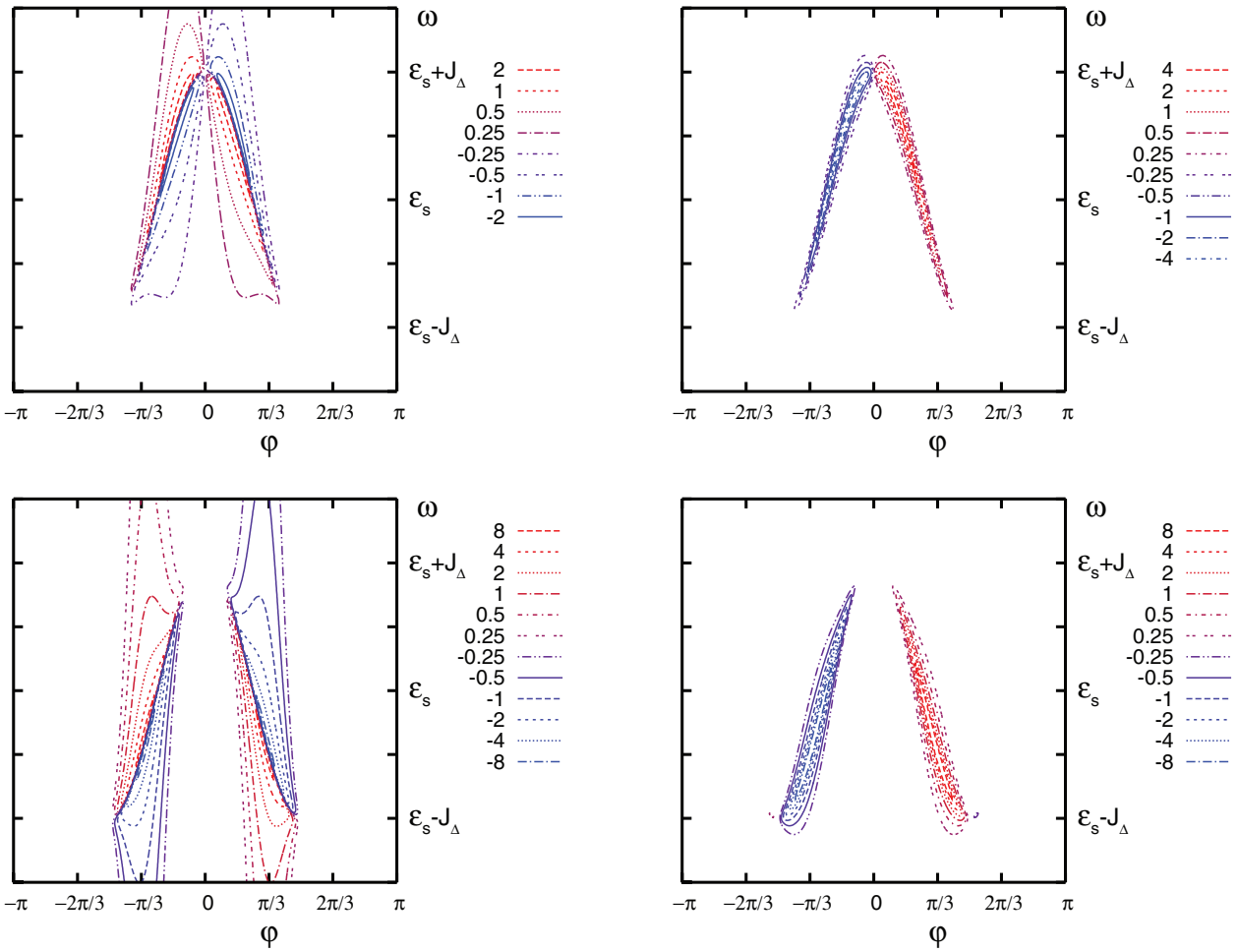

FIG. 3. Top: Angular density of the CD signal of the symmetric exciton $B_+^\dagger$ (Eq. (16)) $\mathcal{I}_{yz}(\omega,\varphi)$ for model (i) with equilibrium width $\sigma=\pi/6$. Left: Real part. Right : Imaginary part. Bottom: the same for model (iii) (with potential minima at $\varphi_0=\pm\pi/3$, and width $\sigma=\pi/12$). Other parameters: $J_\Delta/\Gamma=20$, $\frac{k}{6}R|\tilde{\mu}_z|^2=1$.

contributions vanish. The full $\propto(kR)^2$ signals have many contributions containing electric quadrupole, which give an achiral background. We use a specific combination of tensor components that eliminates this background. The following signal:

$$\mathcal{R}_c \equiv \mathcal{R}^{xx}_{[yz][yz]} + 2\mathcal{R}^{zx}_{[xy][yz]} \tag{18}$$

is a good candidate for probing chiral dynamics. Here, $\mathcal{R}^{zx}$ represents response in a setup where the first two pulses propagate along x, $\vec{k}=(k,0,0)$, and the third pulse and the detection is along z, $\vec{k}=(0,0,k)$. We further defined,

$$\mathcal{R}^{zx}_{[xy][yz]} \equiv \mathcal{R}^{zx}_{xyyz} - \mathcal{R}^{zx}_{yxyz} - \mathcal{R}^{zx}_{xyzy} + \mathcal{R}^{zx}_{yxzy}. \tag{19}$$

The other response function $\mathcal{R}^{xx}$ represents a collinear pulse geometry where all laser pulses propagate along x, $\vec{k}=(k,0,0)$,

$$\mathcal{R}^{xx}_{[yz][yz]} \equiv \mathcal{R}^{xx}_{yzyz} - \mathcal{R}^{xx}_{zyyz} - \mathcal{R}^{xx}_{yzzy} + \mathcal{R}^{xx}_{zyzy}. \tag{20}$$

The antisymmetrization of tensor components is analogous to circular dichroism. Indeed, the signals Eqs. (19) and (20) could be alternatively measured by using circularly left $(-)$ and right $(+)$ polarized pulses, e.g.,

$$\mathcal{R}^{xx}_{[yz][yz]} = \mathcal{R}^{xx}_{++++} - \mathcal{R}^{xx}_{++--} - \mathcal{R}^{xx}_{--++} + \mathcal{R}^{xx}_{----},$$

$$\mathcal{R}^{zx}_{[xy][yz]} = \mathcal{R}^{zx}_{++++} - \mathcal{R}^{zx}_{++--} - \mathcal{R}^{zx}_{--++} + \mathcal{R}^{zx}_{----}. \tag{21}$$

Later we prove that Eq. (18) measured on symmetric state is a good measure of the chirality exchange.

We start with the $\propto(kR)^0$ contribution. This part of response function does not depend on the direction of incoming pulses; i.e., it is same in both $\mathcal{R}^{zx}$ and $\mathcal{R}^{xx}$ pulse setups. Making use of Eq. (F1), we obtain for the signal of the symmetric state $B_+^\dagger$,

$$\mathcal{R}_{\alpha\beta\gamma\delta}(\propto k^0) = \frac{4\tilde{\mu}_z^4}{15}(\delta_{\alpha\beta}\delta_{\gamma\delta}+\delta_{\alpha\gamma}\delta_{\beta\delta}+\delta_{\alpha\delta}\delta_{\gamma\beta}) \times \langle\cos\varphi(\tau_3)\cos\varphi(\tau_2)\cos\varphi(\tau_1)\cos\varphi(0)\rangle_\varphi. \tag{22}$$

This does not show chirality exchange, since it is even in $\varphi(0)$, $\varphi(\tau_1)$, $\varphi(\tau_2)$, and $\varphi(\tau_3)$. The signal is identical in all polarization configurations relevant for $\mathcal{R}^{xx}_{[yz][yz]}$ and vanishes in all polarization configurations relevant for $\mathcal{R}^{zx}_{[xy][yz]}$. Thus, both signals given in Eqs. (19) and (20) vanish identically to order $(kR)^0$,

$$\mathcal{R}^{zx}_{[xy][yz]}(\propto k^0)=0; \qquad \mathcal{R}^{xx}_{[yz][yz]}(\propto k^0)=0.$$

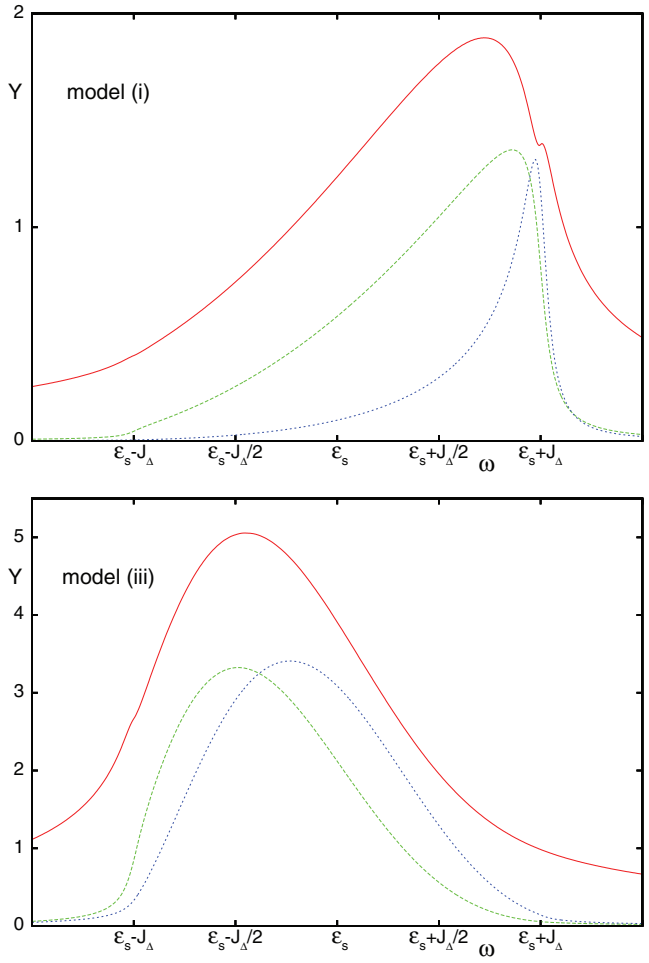

FIG. 4. Integrated absolute values of the signals from Fig. 3. Green dashed line shows integrated real part $\mathrm{Re}\,Y(\omega)$, red solid line shows the integrated imaginary part $\mathrm{Im}\,Y(\omega)$. Absorption line shape $I_{xx}(\omega)$ (blue dotted) is given for comparison.

Similarly, in Appendix D we show that these signals vanish also to order of $(kR)^1$. To complete the argument, the Appendix E shows that the quadratic $k_\beta k_\gamma Y_{\alpha\beta\gamma}$ term of Eq. (10) (electric octupole, magnetic quadrupole) also do not contribute the response up to order $(kR)^2$. The $\propto(kR)^2$ contribution given by Hamiltonian Eq. (8) will thus be the leading term.

Starting with $\mathcal{R}^{zx}$, to lowest order $\propto(kR)^2$, the relevant signals are

$$\begin{aligned}\mathcal{R}^{zx}_{xyzy} &= k^2\langle[\bar{T}^*_{xz}(\tau_3)\bar{\mu}_y(\tau_2)+\bar{\mu}^*_x(\tau_3)\bar{T}_{yz}(\tau_2)]\\ &\quad\times[\bar{T}_{zx}(\tau_1)\bar{\mu}^*_y(0)+\bar{\mu}_z(\tau_1)\bar{T}^*_{yx}(0)]\rangle,\\ \mathcal{R}^{zx}_{yxzy} &= k^2\langle[\bar{T}^*_{yz}(\tau_3)\bar{\mu}_x(\tau_2)+\bar{\mu}^*_y(\tau_3)\bar{T}_{xz}(\tau_2)]\\ &\quad\times[\bar{T}_{zx}(\tau_1)\bar{\mu}^*_y(0)+\bar{\mu}_z(\tau_1)\bar{T}^*_{yx}(0)]\rangle,\\ \mathcal{R}^{zx}_{xyyz} &= k^2\langle[\bar{T}^*_{xz}(\tau_3)\bar{\mu}_y(\tau_2)+\bar{\mu}^*_x(\tau_3)\bar{T}_{yz}(\tau_2)]\\ &\quad\times[\bar{\mu}_y(\tau_1)\bar{T}^*_{zx}(0)+\bar{T}_{yx}(\tau_1)\bar{\mu}^*_z(0)]\rangle,\\ \mathcal{R}^{zx}_{yxyz} &= k^2\langle[\bar{T}^*_{yz}(\tau_3)\bar{\mu}_x(\tau_2)+\bar{\mu}^*_y(\tau_3)\bar{T}_{xz}(\tau_2)]\\ &\quad\times[\bar{\mu}_y(\tau_1)\bar{T}^*_{zx}(0)+\bar{T}_{yx}(\tau_1)\bar{\mu}^*_z(0)]\rangle,\end{aligned}$$

TABLE I. Dipoles and quadrupoles dominating in the $kR\tilde{\mu}\gg\tilde{M}_i,k\tilde{Q}_i$ limit.

$B^\dagger_+$:	$\mu_{+;z}(t)\sim\sqrt{2}\tilde{\mu}_z\cos\varphi$	$B^\dagger_-$:	$\mu_{-;x}(t)\sim\sqrt{2}\tilde{\mu}_x$
	$T_{+;xx}(t)\sim(-i/\sqrt{2})R\tilde{\mu}_x$		$\mu_{-;y}(t)\sim\sqrt{2}\tilde{\mu}_z\sin\varphi$
	$T_{+,yx}(t)\sim(-i/\sqrt{2})R\tilde{\mu}_z\sin\varphi$		$T_{-;zx}(t)\sim(-i/\sqrt{2})R\tilde{\mu}_z\cos\varphi$

where we have used the rules for orientational averaging of Ref. 30 to eliminate terms $k^2\langle\bar{\mu}^*_x(\tau_3)\bar{\mu}_y(\tau_2)\bar{T}_{zx}(\tau_1)\bar{T}^*_{yx}(0)\rangle$ and like from the expansion.

To demonstrate the capacity of the signal Eq. (19) to probe chirality exchange we will assume that the delay time t_2 is much longer than coherence times t_1 and t_3 and the dynamics of φ is slow, so that $\varphi(\tau_3)=\varphi(\tau_2)$ and $\varphi(\tau_1)=\varphi(0)$. Chirality jumps may be ignored during t_1 and t_3 and only take place during the delay time t_2. The signal Eq. (19),

$$\begin{aligned}&\mathcal{R}^{zx}_{[xy][yz]}(t_3,t_2,t_1)\\ &\quad=4k^2\langle\{[-\mathrm{Im}[\bar{T}_{xz}(\tau_2)\bar{\mu}^*_y(\tau_2)]+\mathrm{Im}[\bar{\mu}^*_x(\tau_2)\bar{T}_{yz}(\tau_2)]\}\\ &\qquad\times\{-\mathrm{Im}[\bar{T}_{yx}(0)\bar{\mu}^*_z(0)]+\mathrm{Im}[\bar{\mu}^*_y(0)\bar{T}_{zx}(0)]\}\rangle,\end{aligned}\tag{23}$$

can be obtained by the following average (using the antisymmetry in the indices $\alpha\gamma$ and $\delta\eta$):

$$\begin{aligned}\mathcal{R}^{zx}_{[xy][yz]}(t_3,t_2,t_1)&=4k^2\langle\bar{X}_{xzyyxz}\rangle\\ &=\frac{-4k^2}{210}[7\langle X_{\alpha\alpha\gamma\gamma\xi\xi}\rangle_\varphi+7\langle X_{\alpha\beta\gamma\gamma\beta\alpha}\rangle_\varphi\\ &\quad+28\langle X_{\alpha\beta\gamma\beta\alpha\gamma}\rangle_\varphi]\end{aligned}\tag{24}$$

of the tensor,

$$\begin{aligned}X_{\alpha\beta\gamma\delta\xi\eta}&=\{-\mathrm{Im}[T_{\alpha\beta}(\tau_2)\mu^*_\gamma(\tau_2)]+\mathrm{Im}[\mu^*_\alpha(\tau_2)T_{\gamma\beta}(\tau_2)]\}\\ &\quad\times\{-\mathrm{Im}[T_{\delta\xi}(0)\mu^*_\eta(0)]+\mathrm{Im}[\mu^*_\delta(0)T_{\eta\xi}(0)]\}.\end{aligned}\tag{25}$$

To better understand Eq. (24), we next evaluate it in the limit of negligible internal electric quadrupoles and magnetic dipoles of the groups compared to that induced by the displaced dipoles $kR\tilde{\mu}\gg\tilde{M}_i,k\tilde{Q}_i$ (see Table I for relevant part of T),

$$\begin{aligned}\langle X_{\alpha\alpha\gamma\gamma\xi\xi}\rangle_\varphi&\approx-R^2|\tilde{\mu}_x|^2\tilde{\mu}^2_z\langle\cos\varphi(t_2)\cos\varphi(0)\rangle_\varphi,\\ \langle X_{\alpha\beta\gamma\gamma\beta\alpha}\rangle_\varphi&\approx-2R^2|\tilde{\mu}_x|^2\tilde{\mu}^2_z\langle\cos\varphi(t_2)\cos\varphi(0)\rangle_\varphi\\ &\quad-2R^2\tilde{\mu}^4_z\langle\cos\varphi(t_2)\sin\varphi(t_2)\cos\varphi(0)\sin\varphi(0)\rangle_\varphi,\\ \langle X_{\alpha\beta\gamma\beta\alpha\gamma}\rangle_\varphi&\approx R^2|\tilde{\mu}_x|^2\tilde{\mu}^2_z\langle\cos\varphi(t_2)\cos\varphi(0)\rangle_\varphi.\end{aligned}\tag{26}$$

The contributions $\propto\langle\cos\varphi(t_2)\cos\varphi(0)\rangle_\varphi$ do not identically vanish,

$$\begin{aligned}\mathcal{R}^{zx}_{[xy][yz]}\approx\frac{2(kR)^2}{15}\big\{&2\tilde{\mu}^4_z\langle\cos\varphi(t_2)\sin\varphi(t_2)\cos\varphi(0)\sin\varphi(0)\rangle_\varphi\\ &-|\tilde{\mu}_x|^2\tilde{\mu}^2_z\langle\cos\varphi(t_2)\cos\varphi(0)\rangle_\varphi\big\},\end{aligned}\tag{27}$$

and the chirality jump time scale may not be extracted easily from the $\mathcal{R}^{zx}$ setup, except for $|\mu_x|=0$.

We next consider the leading $\propto(kR)^2$ contribution to the signal for a collinear pulse geometry Eq. (20),

$$\begin{aligned}\mathcal{R}^{xx}_{[yz][yz]} &= 4k^2[\langle \mathrm{Im}[\bar{\mu}^*_y(\tau_2)\bar{\mu}_z(\tau_2)]\mathrm{Im}[\bar{T}^*_{yx}(0)\bar{T}_{zx}(0)]\rangle \\ &+ \langle \mathrm{Im}[\bar{T}^*_{yx}(\tau_2)\bar{T}_{zx}(\tau_2)]\mathrm{Im}[\bar{\mu}^*_y(0)\bar{\mu}_z(0)]\rangle \\ &+ \langle [\mathrm{Im}[\bar{T}_{yx}(\tau_2)\bar{\mu}^*_z(\tau_2)] - \mathrm{Im}[\bar{T}_{zx}(\tau_2)\bar{\mu}^*_y(\tau_2)]] \\ &\times [\mathrm{Im}[\bar{T}_{yx}(0)\bar{\mu}^*_z(0)] - \mathrm{Im}[\bar{T}_{zx}(0)\bar{\mu}^*_y(0)]]\rangle].\end{aligned}$$

The dipole moment element of the symmetric level can be taken to be real. The first two contributions then vanish and the signal is given in terms of the tensor (Eq. (25)),

$$\begin{aligned}\mathcal{R}^{xx}_{[yz][yz]} &= 4k^2\langle \bar{X}_{yxzyxz}\rangle \\ &= \frac{4k^2}{210}[14\langle X_{\alpha\alpha\gamma\gamma\xi\xi}\rangle_\varphi - 21\langle X_{\alpha\beta\gamma\gamma\beta\alpha}\rangle_\varphi \\ &\quad -14\langle X_{\alpha\beta\gamma\beta\alpha\gamma}\rangle_\varphi].\end{aligned}$$

Neglecting the small internal quadrupoles $kR\tilde{\mu} \gg \tilde{M}_i, k\tilde{Q}_i$, we get

$$\begin{aligned}\mathcal{R}^{xx}_{[yz][yz]} \approx \frac{2k^2}{15}\big\{&6R^2\tilde{\mu}_z^4\langle \cos\varphi(t_2)\sin\varphi(t_2)\cos\varphi(0)\sin\varphi(0)\rangle_\varphi \\ &+ 2R^2|\tilde{\mu}_x|^2\tilde{\mu}_z^2\langle \cos\varphi(t_2)\cos\varphi(0)\rangle_\varphi\big\}. \qquad (28)\end{aligned}$$

Similarly to Eq. (27), the monitoring of chiral exchange is complicated by achiral background $\propto\langle\cos\varphi(t_2)\cos\varphi(0)\rangle_\varphi$. Microscopically, it comes from variation of the linear CD signal with molecular orientation.[35–37] For instance, $\mathcal{R}^{xx}_{[yz][yz]}$ represents variation of CD on fixed molecule. Since, for the nonlinear signals, orientational averaging is only applied to (non-negative) quadratic function of CD, it does not vanish for achiral molecules, as in the case of linear chiral probes.

By comparing Eqs. (27) and (28), we find that the chirality jumps can be monitored by the $\mathcal{R}_c$ signal (Eq. (18)),

$$\begin{aligned}\mathcal{R}_c &\equiv \mathcal{R}^{xx}_{[yz][yz]} + 2\mathcal{R}^{zx}_{[xy][yx]} \\ &= \frac{-2k^2}{3}(\langle X_{\alpha\beta\gamma\gamma\beta\alpha}\rangle_\varphi + 2\langle X_{\alpha\beta\gamma\beta\alpha\gamma}\rangle_\varphi) \\ &= \frac{16}{3}\langle \mathrm{Im}[M_z(\tau_2)\mu^*_z(\tau_2)]\mathrm{Im}[M_z(0)\mu^*_z(0)]\rangle_\varphi \\ &\approx \frac{k^2}{3}R^2\tilde{\mu}_z^4\langle \sin 2\varphi(t_2)\sin 2\varphi(0)\rangle_\varphi. \qquad (29)\end{aligned}$$

Similarly we can construct the combination $\mathcal{R}^{xx}_{[yz][yz]} - 2R^{zx}_{[xy][yz]}$ that gives the correlation function $\langle\cos\varphi(t_2)\cos\varphi(0)\rangle_\varphi$. Signals even in φ do not describe chirality switches, but may help to study potential profiles.

Note, that the first two equalities of Eq. (29) are exact, and do not require the neglect of the small internal multipoles $\tilde{M}_i$, $\tilde{Q}_i$. The electric quadrupole does not contribute to the signal, and the achiral background has been completely eliminated. This is in contrast to the two elementary signals $\mathcal{R}^{xx}_{[yz][yz]}$, $R^{zx}_{[xy][zy]}$, where the relatively simple form of Eqs. (27) and (28) only holds for $kR\tilde{\mu} \gg \tilde{M}_i, k\tilde{Q}_i$.

We can understand this finding by extending the arguments given after Eq. (28). Since $\mathcal{R}^{zx}_{[xy][yz]} = \mathcal{R}^{yx}_{[zx][yz]}$, we can recast Eq. (18) as $\mathcal{R}_c = \mathcal{R}^{xx}_{[yz][yz]} + \mathcal{R}^{zx}_{[xy][yz]} + \mathcal{R}^{yx}_{[zx][yz]}$ and interpret $\mathcal{R}_c$ as average of signals from the three directions (along axis x, y, and z) of the third incoming laser pulse (and a local oscillator) of certain sequences of left and right circularly polarized pulses (see Eqs. (21)). These three directions effectively represent orientational averaging $\langle\rangle_o$ after first two pulses, which give rise to the convenient tensor structure $\langle\mu T(t_2)\mu T(0)\rangle_o \to \langle\mu T(t_2)\rangle_o\langle\mu T(0)\rangle_o \to \vec{\mu}\cdot\vec{M}(t_2)\,\vec{\mu}\cdot\vec{M}(0)$.

We next apply these results to the three stochastic models of φ (see Appendices A and C for details),

$$\begin{aligned}\mathcal{R}_c(t_3,t_2,t_1) &= \frac{k^2}{3}R^2\tilde{\mu}_z^4 e^{-\Gamma(t_1+t_3)}e^{i\varepsilon(t_1-t_3)} \\ &\times \int e^{iJ(\varphi')t_1 - iJ(\varphi)t_3}\mathcal{P}(\varphi,\varphi',t_2) \\ &\times \sin 2\varphi'\sin 2\varphi\, d\varphi d\varphi', \qquad (30)\end{aligned}$$

where $\mathcal{P}$ is the two-point joint probability of the stochastic coordinate φ.

For model (ii) (two-state jump) (Eq. (A7)) the integration in Eq. (30) can be carried out analytically,

$$\begin{aligned}\mathcal{R}_c(t_3,t_2,t_1) = \frac{4k^2}{3}R^2\tilde{\mu}_z^4\cos\varphi_0^2\sin^2\varphi_0 e^{-2\Lambda t_2}e^{-\Gamma(t_1+t_3)} \\ \times e^{i(\varepsilon+J(\varphi_0))(t_1-t_3)}.\end{aligned}$$

Frequency-frequency correlation plot $\mathcal{R}_{c,\omega}(\omega_3,t_2,\omega_1) \equiv \mathrm{Re}\int_0^\infty\int_0^\infty \mathcal{R}_c(t_3,t_2,t_1)e^{i(\omega_1 t_1+\omega_3 t_3)}dt_1dt_3$ is displayed in Fig. 5. Jumps between configurations with opposite chirality are not observed in the snapshots of Fig. 5, since the transition frequency does not change during the jump $J(\varphi) = J(-\varphi)$. However, the jump rate is clearly seen in the decay of the peak volume with delay time t_2.

Equation (30) should be combined with Eqs. (A5) and (A8), to get 2D $\mathcal{R}_{c,\omega}$ line shapes for models (i) and (iii) shown in Figs. 6 and 7, respectively. When φ changes continuously (the models (i) and (iii), same parameterization as in Figs. 3 and 4) the transition frequency is varied according to Eq. (3), which affects the line shapes at Figs. 6 and 7. At short delay times $t_2 \to 0$, the angles φ and φ' are correlated $\mathcal{P}(\varphi,\varphi') \to \delta(\varphi-\varphi')\rho_{eq}(\varphi)$ and the 2D peak is elongated along the diagonal. This correlation is lost for longer delay times and the 2D line shapes assume a more circular shape. The line shape is different from the characteristic elliptical 2D line shapes of Gaussian spectral diffusion[38] due to the nonlinear $J(\varphi)$ dependence, and due to weight factor $\sin(2\varphi)$ in Eq. (30). Peak positions and profiles along the diagonal correspond to the integrated angular densities of Fig. 4 (note the broad peak of Fig. 6 vs. the narrow peak of absorption line shape in Fig. 4). Comparing the 2D and absorption line shapes may thus allow to experimentally determine the free energy potential of φ.

The response function, $\mathcal{R}_C(t_2) \equiv \mathcal{R}_c(0,t_2,0)$, constitutes a direct measure of chirality exchange. In fact, we have already looked at it, because it corresponds to the peak volume of 2D spectra $\mathcal{R}_C(t_2) = \int d\omega_1 d\omega_3 \mathcal{R}_{c,\omega}(\omega_3,t_2,\omega_1)$. Alternatively, it can also be measured directly by keeping intervals t_1 and t_3 small, but holding pulses time-ordered. The evolution of the peak volume is displayed in Fig. 8 (see Appendix G for derivation). The line shape decays

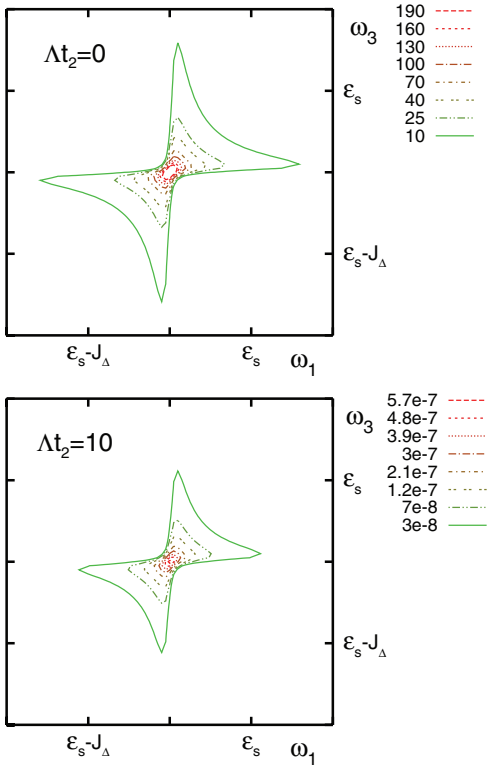

FIG. 5. Chiral photon echo signal $\mathcal{R}_{c,\omega}$ (Eq. (30)) of the symmetric exciton level of a dimer undergoing a two-state jump (model (ii)) between configurations with opposite chirality (Eq. (A7)). Shown are the frequency-frequency correlation plots $\mathcal{R}_{c,\omega}(\omega_3, t_2, \omega_1)$ at two delay times as indicated. Other parameters: $\varphi_0 = \pi/3.0$, $J_\Delta/\Gamma = 20$, $\frac{k^2}{3}R^2|\tilde{\mu}_z|^4 = 1$.

exponentially $\propto e^{-2\Lambda t_2}$ for model (ii) (Eq. (G3)) and almost exponentially $\propto \sinh(4\sigma^2 e^{-Dt_2}) \approx 4\sigma^2 e^{-Dt_2}$ for model (i) (Eq. (G2)). Model (iii) (Eq. (G4)) shows a two-stage decay. First, the φ is equilibrated $\propto e^{-Dt_2}$ inside one well, then, the decay slows down to represent transition over the barrier $\propto e^{-2\Lambda t_2}$.

B. Signatures of chirality exchange in the 2D spectrum of the antisymmetric exciton

The transition dipole of the antisymmetric state $B_-^\dagger$ is much weaker than that of $B_+^\dagger$ and has a minimum in the non-chiral configuration $\varphi = 0$. Here, we show that some signatures of chirality dynamics can be found even in the $\propto(kR)^0$ signal. Such signals also exist in non-chiral molecules so they are not chirality specific. However, since the dipoles depend on φ, it will be interesting to examine whether the dynamical chirality can be monitored by the non-chiral $\propto(kR)^0$ signal.

A full analysis of all tensor components of this signal in the slow dynamics limit $\varphi(\tau_3) = \varphi(\tau_2)$ and $\varphi(\tau_1) = \varphi(0)$ is presented in Appendix F. The chiral dynamics must be represented by correlation functions such as $\langle \sin\varphi(\tau_2)\sin\varphi(0)\rangle_\varphi$. Chirality is thus best monitored by the following signal $\mathcal{R}_d(t_3, t_2, t_1) \equiv \mathcal{R}_{yyzz}(t_3, t_2, t_1) - \mathcal{R}_{yzyz}(t_3, t_2, t_1)$:

$$\mathcal{R}_d(t_3, t_2, t_1) = \frac{2}{3}|\tilde{\mu}_x|^2\tilde{\mu}_z^2[\langle \sin^2\varphi(t_2)\rangle_\varphi + \langle \sin^2\varphi(0)\rangle_\varphi - 2\langle \sin\varphi(t_2)\sin\varphi(0)\rangle_\varphi]. \quad (31)$$

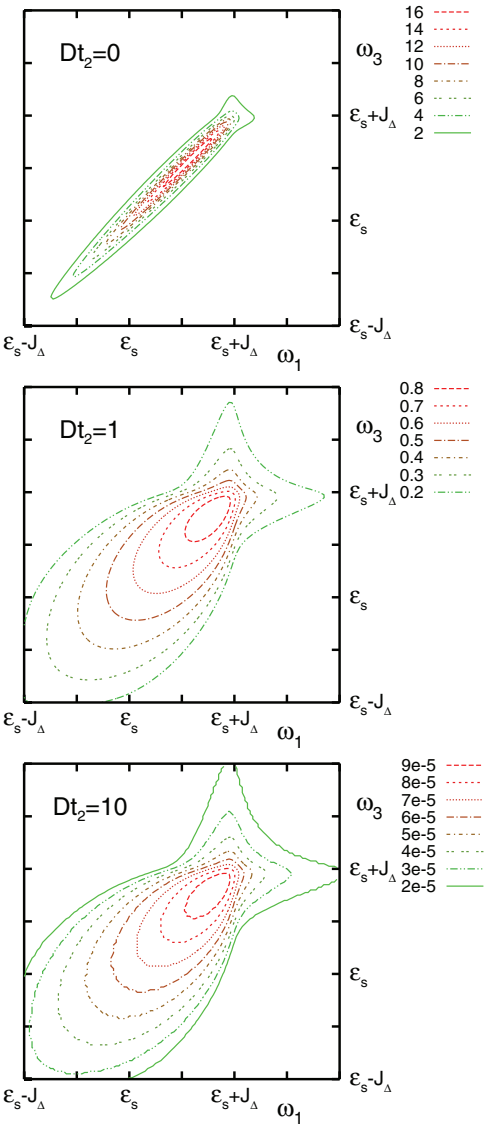

FIG. 6. Same as Fig. 5 but for model (i) (Eq. (A5)) at delay times $Dt_2 = 0$ (top panel), $Dt_2 = 1$ (central panel), and $Dt_2 = 10$ (bottom panel). Parameters: $\sigma = \pi/6$, $J_\Delta/\Gamma = 20$, $\frac{k^2}{3}R^2|\tilde{\mu}_z|^4 = 1$.

Signals of the antisymmetric exciton are of interest provided $\tilde{\mu}_z \neq 0$, and $\tilde{\mu}_x \neq 0$. We note that $\mathcal{R}_d$ of the symmetric state vanishes. The signal is not related to correlations of the pseudoscalar $\mu \cdot M$, but since the dipoles depend on φ it allows to monitor the dynamical chirality by stronger signal $\propto(kR)^0$.

Making use of Eq. (C2), we get from Eq. (31),

$$\mathcal{R}_d(t_3, t_2, t_1) = \frac{2}{3}|\tilde{\mu}_x|^2\tilde{\mu}_z^2 e^{i\varepsilon(t_1-t_3)-\Gamma(t_1+t_3)} \times \int e^{iJ(\varphi)t_3 - iJ(\varphi')t_1}\mathcal{P}(\varphi, \varphi', t_2) \times (\sin\varphi - \sin\varphi')^2\, d\varphi d\varphi'. \quad (32)$$

The chirality dynamics is well represented by the $\mathcal{R}_D(t_2) \equiv \mathcal{R}_d(t_3 = 0, t_2, t_1 = 0)$ signal. The evolution of $\mathcal{R}_d$ with the delay time t_2 is analyzed in Eqs. (G5)–(G7). $\mathcal{R}_D = 0$ at $t_2 = 0$ and increases to asymptotic value $\mathcal{R}_D = (4/3)|\tilde{\mu}_x|^2\tilde{\mu}_z^2\langle \sin^2\varphi\rangle_\varphi$ at $t_2 = \infty$. The variation of

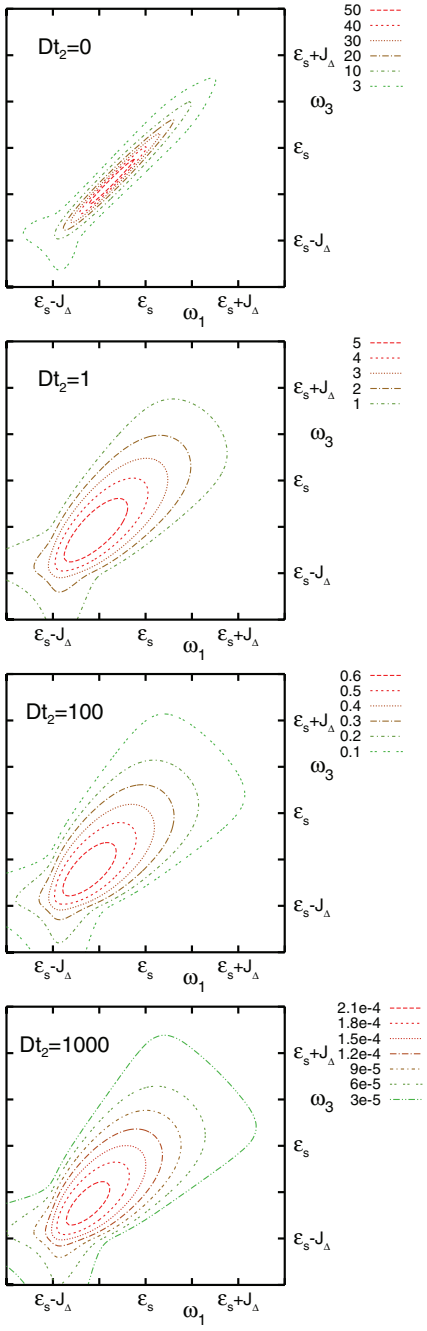

FIG. 7. Same as Fig. 5 but for model (iii) (Eq. (A8)) at delay times (from top to bottom) $Dt_2 = 0$, 1, 100, 1000. Parameters: $\Lambda/D = 0.01$, $\varphi_0 = \pi/3.0$, $\sigma = \pi/12.0$, $J_\Delta/\Gamma = 20$, $\frac{k^2}{3}R^2|\tilde{\mu}_z|^4 = 1$.

$\{\mathcal{R}_D(\infty) - \mathcal{R}_D(t_2)\}/\mathcal{R}_D(\infty)$ on a logarithmic scale vs. t_2 is shown in Fig. 9. The slopes of this graph provide the rates Λ and D similar to what was done in the discussion of Fig. 8. We thus found signatures of the dynamics of φ already in the $\propto(kR)^0$ signal.

We note, that $\mathcal{R}_d = 0$ for the symmetric exciton (see Eq. (22)); the line shape along the diagonal will thus be dominated by Eq. (32). The signal $\mathcal{R}_d$ thus will be helpful, even when the symmetric and antisymmetric exciton spectra overlap; full account of cross peaks is nevertheless necessary. We should bear in mind, however, that the $\mathcal{R}_d$ signal is finite in non-chiral molecules so that this probe is not chirality

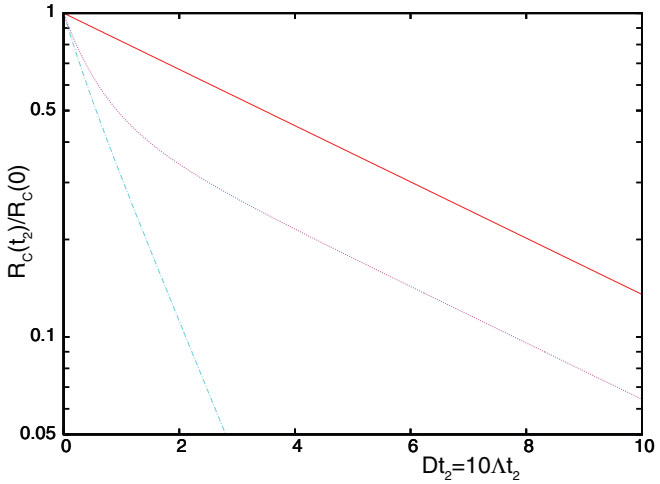

FIG. 8. Decay of the peak volume $\mathcal{R}_C \equiv \int d\omega_3 d\omega_1 \mathcal{R}(\omega_3, t_2, \omega_1)$ with delay time t_2 for model (i) (Eq. (G2), blue dashed-dotted line), model (ii) (Eq. (G3), red solid line), and model (iii) (Eq. (G4), magenta dotted line). Straight lines indicate exponential decay. Parameters: $\Lambda/D = 0.1$, $\varphi_0 = \pi/3.0$, $\sigma = \pi/6.0$.

specific. Also, the need to subtract the asymptotic values will reduce the accuracy of the measurement.

In conclusion, we have designed two nonlinear optical signals that contain clear signatures of ultrafast chiral exchange and fluctuations in dimers with axial chirality. Our conclusions are not limited to the Frenkel exciton model with dipole-dipole coupling used here. They hold as long as we can spectrally select single excited level, the ground and excited states hold the symmetric properties of our model, the coupling term is even in φ, and the multipoles follow the standard geometric tensor transformations of Appendix B.

The $\mathcal{R}_c$ signal is related to the pseudoscalar $\vec{\mu}\cdot\vec{M}$ — the established measure of molecular chirality. The subtractions in Eqs. (19) and (20), and the strict prescription for directions and polarizations of laser pulses suggest, that differential measurements and phase cycling[21] may be effective

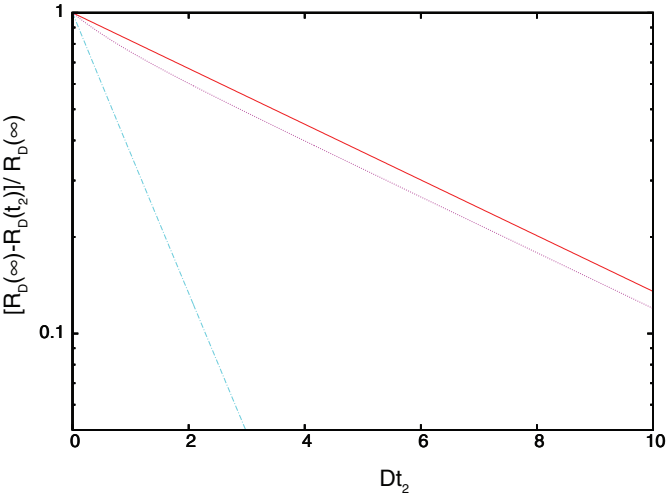

FIG. 9. Variation of the signal $\mathcal{R}_D(t_2)$ with delay time t_2 for model (i) (Eq. (G5), blue dashed-dotted line), model (ii) (Eq. (G6), red solid line), and model (iii) (Eq. (G7), magenta dotted line). Straight lines indicate exponential decay. Parameters: $\Lambda/D = 0.1$, $\varphi_0 = \pi/3.0$, $\sigma = \pi/6.0$.

in implementation of the photon echo signal. Similar combinations of pulse polarizations can be also used to monitor axial chirality by the non-rephasing pulse sequence.[32] However, the control over pulse time ordering must be kept: the commonly used addition of the rephasing (photon echo) and non-rephasing signals[39,40] will not work here, since the relevant tensor indices in Eqs. (19) and (20) are antisymmetric (and the sum tends to vanish).

The specificity of the other signal $\mathcal{R}_d$ for probing chiral exchange is somewhat less theoretically sound, but under our model assumptions it shows similar correlation of angle φ as $\mathcal{R}_c$ does. It is much stronger than $\mathcal{R}_d$ and can be reached with today's laser technology.

There are some limitations to our conclusions. The reflection symmetry can be violated also by fluctuating energetic parameters rather than by molecular geometry. For instance, we have neglected static disorder or spectral diffusion, which can alter the B_+, B_- eigenbasis in the course of time and induce the transfer between the two states.[41] In particular, it has been reported that the antisymmetric state can acquire transition moment due to spectral diffusion[42] and thus may affect the $\mathcal{R}_d$ signal at short delay times even without geometric fluctuations. One must thus control over other sources of asymmetry with respect to reflection.

ACKNOWLEDGMENTS

We gratefully acknowledge the support of the National Science Foundation (NSF) through Grant No. CHE-1058791, from the National Institutes of Health (NIH) through Grant Nos. GM-59230 and GM091364, and the Defense Advanced Research Projects Agency, Grant No. UOFT-49606. Support of the Czech Science Foundation (GACR) Grant No. 205/10/0898 and research plan MSM0021620835 of the Ministry of Education, Youth, and Sports of the Czech Republic is also acknowledged. The authors are indebted to Professor David Beratan for most useful discussions and Václav Perlík for help with Fig. 1.

APPENDIX A: DYNAMICAL MODELS OF CHIRALITY

We describe the stochastic dynamics of $\varphi(t)$ by the Markovian master equation for the density,[43]

$$\frac{\partial \rho(\varphi, t)}{\partial t} = \mathcal{L}\rho(\varphi, t), \tag{A1}$$

where $\mathcal{L}$ is an operator in φ space. Equation (A1) must be solved with the boundary condition $\rho(\varphi, 0) = \delta(\varphi - \varphi')$ to get Green's function $\mathcal{G}(\varphi, \varphi', t)$. The equilibrium density $\rho^{\mathrm{eq}}(\varphi)$ (normalized to $\int \rho^{\mathrm{eq}}(\varphi) d\varphi = 1$) can be obtained by the setting the lhs of Eq. (A1) to zero. The Green's function and the equilibrium density will be combined to get two time joint probability densities required in Eq. (30),

$$\mathcal{P}(\varphi, \varphi', t) = \mathcal{G}(\varphi, \varphi', t)\rho^{\mathrm{eq}}(\varphi'). \tag{A2}$$

We introduce three dynamical models of $\varphi(t)$ as shown in Fig. 2.

1. Model (i): Diffusion in a harmonic potential

We assume that φ undergoes diffusion in harmonic potential $U = U''\varphi^2/2$ around $\varphi = 0$. This Ornstein-Uhlenbeck process[44] is described by Smoluchowski equation,[45]

$$\frac{\partial \rho(\varphi, t)}{\partial t} = D\left[\frac{\partial^2}{\partial \varphi^2} + \frac{\partial}{\partial \varphi}\frac{\varphi}{\sigma^2}\right]\rho(\varphi, t), \tag{A3}$$

where $\sigma^2 = k_B T/U''$, T is the temperature, and k_B is the Boltzmann constant. The diffusion constant D is the inverse autocorrelation time of fluctuations around the achiral stable conformation. Limit $\sigma \to \infty$ represents free diffusion in φ space.

The equilibrium density is

$$\rho^{\mathrm{eq}}_{(\mathrm{i})}(\varphi) = \frac{1}{\sigma\sqrt{2\pi}} \exp\left[-\frac{\varphi^2}{2\sigma^2}\right], \tag{A4}$$

and the two-point joint probability density (Eq. (A2)) is given by

$$\mathcal{P}_{(\mathrm{i})}(\varphi, \varphi', t) = \frac{1}{2\sigma^2\pi\sqrt{1 - e^{-2Dt}}} \times \exp\left[-\frac{\varphi^2 + \varphi'^2 - 2\varphi\varphi' e^{-Dt}}{2\sigma^2(1 - e^{-2Dt})}\right]. \tag{A5}$$

2. Model (ii): Two-state chirality-jump model

The two-state jump dynamics has been introduced in the spectroscopy by Kubo and Anderson as an exactly solvable model of spectral diffusion with arbitrary time scale.[46–48] Here, the two states represent orientations of dipoles in space in the spirit of Ref. 49.

The dihedral angle can assume two values $\varphi = \varphi_0$ and $-\varphi_0$ representing conformations with opposite chirality. The exchange dynamics is described by a Markovian master equation (A1) for the probability density of the two states φ_0, $-\varphi_0$ (Ref. 46) with symmetric transition rate Λ,

$$\frac{d}{dt}\begin{pmatrix}\rho(\varphi_0)\\ \rho(-\varphi_0)\end{pmatrix} = \begin{pmatrix}-\Lambda & \Lambda\\ \Lambda & -\Lambda\end{pmatrix}\begin{pmatrix}\rho(\varphi_0)\\ \rho(-\varphi_0)\end{pmatrix}. \tag{A6}$$

The equilibrium density is $\rho^{\mathrm{eq}}_{(\mathrm{ii})} = [\delta(\varphi - \varphi_0) + \delta(\varphi + \varphi_0)]/2$ and the two-time joint probability density (Eq. (A2)) is

$$\begin{aligned}\mathcal{P}_{(\mathrm{ii})}(\varphi, \varphi', t) = {} & \frac{1 + e^{-2\Lambda t}}{4}[\delta(\varphi - \varphi_0)\delta(\varphi' - \varphi_0) \\ & + \delta(\varphi + \varphi_0)\delta(\varphi' + \varphi_0)] \\ & + \frac{1 - e^{-2\Lambda t}}{4}[\delta(\varphi + \varphi_0)\delta(\varphi' - \varphi_0) \\ & + \delta(\varphi - \varphi_0)\delta(\varphi' + \varphi_0)].\end{aligned} \tag{A7}$$

Equation (A7) will be used in Eq. (30).

3. Model (iii): Diffusion in a double-well potential

Diffusion in a double-well potential can be approximated by a combination of two-state jump between wells and diffusion in two harmonic wells with potential minima at $-\varphi_0$ and φ_0. We assume that transition over barrier is the two-state

jump model of Sec. A2 with transition rate (see Eq. XII (2.2.) in Ref. 43)

$$\Lambda = \frac{D}{\sqrt{2\pi}}\sqrt{-U''(\varphi_0)U''(0)}\exp\left[\frac{U(\varphi_0)-U(0)}{kT}\right].$$

We next assume that the deviation from the minima $\varphi \pm \varphi_0$ in the wells after the transition is uncorrelated with its prior position; relaxation in the well is thus much faster than transition over large barrier, which is a realistic assumption. Distribution of φ after jump always follows (local) equilibrium densities in the wells $\rho^{\rm eq}_{\rm (i)}(\varphi \pm \varphi_0)$ (Eq. (A4)). The joint two-point probability densities are then products of local equilibrium densities.

The fraction of the trajectories will not cross the barrier over the specified time period. In this case we can use Eq. (A5) shifted by $\pm\varphi_0$. Equation (A2) then reads as

$$\begin{aligned}\mathcal{P}_{\rm (iii)}(\varphi,\varphi',t) = {}& \frac{e^{-\Lambda t}}{2}[\mathcal{P}_{\rm (i)}(\varphi-\varphi_0,\varphi'-\varphi_0,t)\\ &+\mathcal{P}_{\rm (i)}(\varphi+\varphi_0,\varphi'+\varphi_0,t)]\\ &+\frac{(1-e^{-\Lambda t})^2}{4}\left[\rho^{\rm eq}_{\rm (i)}(\varphi-\varphi_0)\rho^{\rm eq}_{\rm (i)}(\varphi'-\varphi_0)\right.\\ &\left.+\rho^{\rm eq}_{\rm (i)}(\varphi+\varphi_0)\rho^{\rm eq}_{\rm (i)}(\varphi'+\varphi_0)\right]\\ &+\frac{1-e^{-2\Lambda t}}{4}\left[\rho_{\rm (i)}(\varphi+\varphi_0)\rho^{\rm eq}_{\rm (i)}(\varphi'-\varphi_0)\right.\\ &\left.+\rho^{\rm eq}_{\rm (i)}(\varphi-\varphi_0)\rho_{\rm (i)}(\varphi'+\varphi_0)\right]. \qquad \text{(A8)}\end{aligned}$$

Eqations (A8) reduces to Eq. (A7) for $\sigma \to 0$ and Eq. (A5) for $\varphi_0 = 0$, $\Lambda \to 0$.

The following approximation for equilibrium density:

$$\rho^{\rm eq}_{\rm (iii)}(\varphi) = \left[\rho^{\rm eq}_{\rm (i)}(\varphi+\varphi_0)+\rho^{\rm eq}_{\rm (i)}(\varphi-\varphi_0)\right]/2 \qquad \text{(A9)}$$

is consistent with Eq. (A8) since $\mathcal{P}_{\rm (iii)}(\varphi,\varphi',t\to\infty) = \rho^{\rm eq}_{\rm (iii)}(\varphi)\rho^{\rm eq}_{\rm (iii)}(\varphi')$.

APPENDIX B: INTERNAL MAGNETIC DIPOLES AND ELECTRIC QUADRUPOLES

The complete Hamiltonian to first order in k includes the internal magnetic dipoles and electric quadrupoles of each molecular group. Here, we summarize their reflection and transformation properties. The magnetic dipole is an axial vector so that $\vec{M}_1|_{\varphi=0} = (\tilde{M}_x, \tilde{M}_y, \tilde{M}_z)$ and $\vec{M}_2|_{\varphi=0} = (\tilde{M}_x, -\tilde{M}_y, -\tilde{M}_z)$. Its transformation under φ twist is given by

$$\begin{aligned}\vec{M}_1 &= (\tilde{M}_x, \tilde{M}_y\cos\varphi + \tilde{M}_z\sin\varphi, \tilde{M}_z\cos\varphi - \tilde{M}_y\sin\varphi),\\ \vec{M}_2 &= (\tilde{M}_x, -\tilde{M}_y\cos\varphi + \tilde{M}_z\sin\varphi, -\tilde{M}_z\cos\varphi - \tilde{M}_y\sin\varphi).\end{aligned} \qquad \text{(B1)}$$

Similarly the electric quadrupole is a symmetric tensor,

$$\overleftrightarrow{Q}_1|_{\varphi=0} = \begin{pmatrix}\tilde{Q}_{xx} & \tilde{Q}_{xy} & \tilde{Q}_{xz}\\ \tilde{Q}_{xy} & \tilde{Q}_{yy} & \tilde{Q}_{yz}\\ \tilde{Q}_{xz} & \tilde{Q}_{yz} & \tilde{Q}_{zz}\end{pmatrix},$$

$$\overleftrightarrow{Q}_2|_{\varphi=0} = \begin{pmatrix}\tilde{Q}_{xx} & -\tilde{Q}_{xy} & -\tilde{Q}_{xz}\\ -\tilde{Q}_{xy} & \tilde{Q}_{yy} & \tilde{Q}_{yz}\\ -\tilde{Q}_{xz} & \tilde{Q}_{yz} & \tilde{Q}_{zz}\end{pmatrix}$$

with the transformation,

$$\overleftrightarrow{Q}_1 = \begin{pmatrix}\tilde{Q}_{xx} & \tilde{Q}_{xy}\cos(\varphi)+\tilde{Q}_{xz}\sin(\varphi) & \tilde{Q}_{xz}\cos(\varphi)-\tilde{Q}_{xy}\sin(\varphi)\\ \tilde{Q}_{xy}\cos(\varphi)+\tilde{Q}_{xz}\sin(\varphi) & \tilde{Q}_{yy}\cos^2(\varphi)+\tilde{Q}_{zz}\sin^2(\varphi)+\tilde{Q}_{yz}\sin(2\varphi) & \tilde{Q}_{yz}\cos(2\varphi)+[\tilde{Q}_{zz}-\tilde{Q}_{yy}]\sin(2\varphi)/2\\ \tilde{Q}_{xz}\cos(\varphi)-\tilde{Q}_{xy}\sin(\varphi) & \tilde{Q}_{yz}\cos(2\varphi)+[\tilde{Q}_{zz}-\tilde{Q}_{yy}]\sin(2\varphi)/2 & \tilde{Q}_{zz}\cos^2(\varphi)+\tilde{Q}_{yy}\sin^2(\varphi)-\tilde{Q}_{yz}\sin(2\varphi)\end{pmatrix},$$

$$\overleftrightarrow{Q}_2 = \begin{pmatrix}\tilde{Q}_{xx} & -\tilde{Q}_{xy}\cos(\varphi)+\tilde{Q}_{xz}\sin(\varphi) & -\tilde{Q}_{xz}\cos(\varphi)-\tilde{Q}_{xy}\sin(\varphi)\\ -\tilde{Q}_{xy}\cos(\varphi)+\tilde{Q}_{xz}\sin(\varphi) & \tilde{Q}_{yy}\cos^2(\varphi)+\tilde{Q}_{zz}\sin^2(\varphi)-\tilde{Q}_{yz}\sin(2\varphi) & \tilde{Q}_{yz}\cos(2\varphi)-[\tilde{Q}_{zz}-\tilde{Q}_{yy}]\sin(2\varphi)/2\\ -\tilde{Q}_{xz}\cos(\varphi)-\tilde{Q}_{xy}\sin(\varphi) & \tilde{Q}_{yz}\cos(2\varphi)-[\tilde{Q}_{zz}-\tilde{Q}_{yy}]\sin(2\varphi)/2 & \tilde{Q}_{zz}\cos^2(\varphi)+\tilde{Q}_{yy}\sin^2(\varphi)+\tilde{Q}_{yz}\sin(2\varphi)\end{pmatrix}.$$

We next show how these internal multipoles contribute to the interaction Hamiltonian in the $B_\pm$ basis. The magnetic dipole part of Eq. (4) is given by

$$\sum_{j=1,2} B_j^\dagger \vec{M}_j e^{i(-1)^j\vec{k}\cdot\vec{R}/2} = \frac{1}{2}\left[\left(\vec{M}_1+\vec{M}_2\right)\left(B_1^\dagger+B_2^\dagger\right)\right.$$
$$\left.+\left(\vec{M}_1-\vec{M}_2\right)\left(B_1^\dagger-B_2^\dagger\right)\right]+\mathcal{O}(k). \qquad \text{(B2)}$$

Its contribution to the total magnetic dipole,

$$\begin{aligned}\vec{M}_+ &= \frac{1}{\sqrt{2}}\left[\vec{M}_1+\vec{M}_2\right]+\vec{M}_{1\leftrightarrow2,+}\\ &= \sqrt{2}(\tilde{M}_x, \tilde{M}_z\sin(\varphi), -[\tilde{M}_y + i(kR\tilde{\mu}_z/4)]\sin(\varphi))\\ \vec{M}_- &= \frac{1}{\sqrt{2}}\left[\vec{M}_1-\vec{M}_2\right]+\vec{M}_{1\leftrightarrow2,-}\\ &= \sqrt{2}(0, [\tilde{M}_y + i(kR\tilde{\mu}_z/4)]\cos(\varphi), \tilde{M}_z\cos(\varphi)),\end{aligned} \qquad \text{(B3)}$$

The electric quadrupole part of Eq. (4),

$$\sum_{j=1,2} B_j^\dagger \overleftrightarrow{Q}_j e^{i(-1)^j \vec{k}\cdot\vec{R}/2} = \frac{1}{2}\left[\left(\overleftrightarrow{Q}_1 + \overleftrightarrow{Q}_2\right)\left(B_1^\dagger + B_2^\dagger\right) + \left(\overleftrightarrow{Q}_1 - \overleftrightarrow{Q}_2\right)\left(B_1^\dagger - B_2^\dagger\right)\right] + \mathcal{O}(k),$$

contributes to the total electric quadrupole,

$$\overleftrightarrow{Q}_+ = \frac{1}{\sqrt{2}}\left[\overleftrightarrow{Q}_1 + \overleftrightarrow{Q}_2\right] + \overleftrightarrow{Q}_{1\leftrightarrow 2,+}$$

$$= \sqrt{2}\begin{pmatrix} \tilde{Q}_{xx} - (R\tilde{\mu}_x/2) & [\tilde{Q}_{xz} - (R\tilde{\mu}_z/4)]\sin(\varphi) & -\tilde{Q}_{xy}\sin(\varphi) \\ \sin(\varphi)[\tilde{Q}_{xz} - (R\tilde{\mu}_z/4)] & \tilde{Q}_{yy}\cos^2(\varphi) + \tilde{Q}_{zz}\sin^2(\varphi) & \tilde{Q}_{yz}\cos(2\varphi) \\ -\tilde{Q}_{xy}\sin(\varphi) & \tilde{Q}_{yz}\cos(2\varphi) & \tilde{Q}_{zz}\cos^2(\varphi) + \tilde{Q}_{yy}\sin^2(\varphi) \end{pmatrix},$$

$$\overleftrightarrow{Q}_- = \frac{1}{\sqrt{2}}\left[\overleftrightarrow{Q}_1 - \overleftrightarrow{Q}_2\right] + \overleftrightarrow{Q}_{1\leftrightarrow 2,-}$$

$$= \sqrt{2}\begin{pmatrix} 0 & \tilde{Q}_{xy}\cos(\varphi) & [\tilde{Q}_{xz} - (R\tilde{\mu}_z/4)]\cos(\varphi) \\ \tilde{Q}_{xy}\cos(\varphi) & \tilde{Q}_{yz}\sin(2\varphi) & [\tilde{Q}_{zz} - \tilde{Q}_{yy}]\sin(2\varphi)/2 \\ \cos(\varphi)[\tilde{Q}_{xz} - (R\tilde{\mu}_z/4)] & [\tilde{Q}_{zz} - \tilde{Q}_{yy}]\sin(2\varphi)/2 & -\tilde{Q}_{yz}\sin(2\varphi) \end{pmatrix}.$$

These complete multipoles may be used to calculate the full signals.

APPENDIX C: THE STOCHASTIC LIOUVILLE EQUATION

The path integration $\langle\rangle_\varphi$ required for the evaluation of response function in the molecular frame can be conveniently calculated using a representation in φ space. In this space $\mathcal{J}_\alpha(\varphi)$ have to be represented by a diagonal operator $\hat{\mathcal{J}}_\alpha\hat{\rho} = \mathcal{J}_\alpha(\varphi)\rho(\varphi)$. Similarly, $\hat{J}$ is diagonal operator of couplings (Eq. (3)) $\hat{J}\hat{\rho} = J(\varphi)\rho(\varphi)$. Notably, in the two-state model (ii) $J(\varphi_0) = J(-\varphi_0)$ and $\hat{J}$ becomes c-number. Evolution during time intervals t_1, t_2, t_3 of the 3-rd order response is described by stochastic Liouville equation,[33,34]

$$\frac{d\hat{\rho}}{dt} = i\eta(\varepsilon \pm \hat{J})\hat{\rho} - \eta^2\Gamma\hat{\rho} + \hat{\mathcal{L}}\hat{\rho},$$

where $\hat{\mathcal{L}}$ represents master equation of the Markovian stochastic process (Eq. (A1)). The upper sign applies to symmetric exciton state and lower sign to antisymmetric exciton. C-number η depends on Liouville space state and becomes (for the photon echo experiment) $\eta = 1$ in the t_1 interval , $\eta = -1$ in the t_3 interval, and $\eta = 0$ in the t_2 interval. For linear response $\eta = -1$.

The linear response function (Eq. (12)) requires the evaluation of the following average:

$$\langle\mathcal{J}_\alpha^*(t)\mathcal{J}_\beta(0)\rangle_\varphi = e^{-i\varepsilon t - \Gamma t}\hat{I}\hat{\mathcal{J}}_\alpha^* e^{(\mp i\hat{J} + \hat{\mathcal{L}})t}\hat{\mathcal{J}}_\beta\hat{\rho}^{\mathrm{eq}},$$

where $\hat{\rho}^{\mathrm{eq}}$ are the equilibrium densities (solution to Eq. (A1) with zero l.h.s.) and $\hat{I}$ is the final summation over all φ states $\hat{I}\hat{\rho} = \int \rho(\varphi)d\varphi$.

The third-order response function shall be calculated using

$$\langle\mathcal{J}_\alpha^*(\tau_3)\mathcal{J}_\beta(\tau_2)\mathcal{J}_\gamma(\tau_1)\mathcal{J}_\delta^*(0)\rangle_\varphi = e^{i\varepsilon(t_1-t_3)-\Gamma(t_1+t_3)}\hat{I}\hat{\mathcal{J}}_\alpha^* e^{(\mp i\hat{J}+\hat{\mathcal{L}})t_3}\hat{\mathcal{J}}_\beta e^{\hat{\mathcal{L}}t_2}\hat{\mathcal{J}}_\gamma e^{(\pm i\hat{J}+\hat{\mathcal{L}})t_1}\hat{\mathcal{J}}_\delta^*\hat{\rho}^{\mathrm{eq}}.$$

To describe the slow φ dynamics we approximate the dynamics in the first and third interval by $e^{(\mp i\hat{J}+\hat{\mathcal{L}})t_3} \approx e^{\mp i\hat{J}t_3}$, and $e^{(\pm i\hat{J}+\hat{\mathcal{L}})t_1} \approx e^{\pm i\hat{J}t_1}$, respectively. The linear response is then obtained by orientational averaging of

$$\langle\mathcal{J}_\alpha^*(t)\mathcal{J}_\beta(0)\rangle_\varphi = e^{-i\varepsilon t-\Gamma t}\int e^{\mp iJ(\varphi)t}\mathcal{J}_\alpha^*(\varphi)\mathcal{J}_\beta(\varphi)\rho^{\mathrm{eq}}(\varphi)d\varphi. \tag{C1}$$

Since $e^{\hat{\mathcal{L}}t_2} = \mathcal{G}$ is the Green function of Eq. (A1), and taking into account Eq. (A2), we get

$$\langle\mathcal{J}_\alpha^*(\tau_3)\mathcal{J}_\beta(\tau_2)\mathcal{J}_\gamma(\tau_1)\mathcal{J}_\delta^*(0)\rangle_\varphi = e^{i\varepsilon(t_1-t_3)-\Gamma(t_1+t_3)}\int e^{\pm iJ(\varphi')t_1 \mp iJ(\varphi)t_3}\mathcal{P}(\varphi,\varphi',t_2) \times \mathcal{J}_\alpha^*(\varphi)\mathcal{J}_\beta(\varphi)\mathcal{J}_\gamma(\varphi')\mathcal{J}_\delta^*(\varphi')d\varphi d\varphi'. \tag{C2}$$

Upon orientational averaging this leads to Eqs. (30) and (32).

APPENDIX D: ANALYSIS OF ~(*kR*) SCALING NONLINEAR SIGNALS

The contribution of both magnetic dipole and electric quadrupole can be conveniently calculated in a single step by using Eqs. (8) and (10),

$$H(\propto kR) = E_\alpha k_\beta T_{\alpha\beta} B^\dagger + h.c.$$

Evaluation of $\propto(kR)$ terms of the third-order response functions,

$$\begin{aligned}\mathcal{R}_{\alpha\beta\gamma\delta}(\propto kR) = k_{4;\eta}\langle\bar{T}^*_{\alpha\eta}(\tau_3)\bar{\mu}_\beta(\tau_2)\bar{\mu}_\gamma(\tau_1)\bar{\mu}^*_\delta(0)\rangle \\ + k_{3;\eta}\langle\bar{\mu}^*_\alpha(\tau_3)\bar{T}_{\beta\eta}(\tau_2)\bar{\mu}_\gamma(\tau_1)\bar{\mu}^*_\delta(0)\rangle \\ + k_{2;\eta}\langle\bar{\mu}^*_\alpha(\tau_3)\bar{\mu}_\beta(\tau_2)\bar{T}_{\gamma\eta}(\tau_1)\bar{\mu}^*_\delta(0)\rangle \\ + k_{1;\eta}\langle\bar{\mu}^*_\alpha(\tau_3)\bar{\mu}_\beta(\tau_2)\bar{\mu}_\gamma(\tau_1)\bar{T}^*_{\delta\eta}(0)\rangle,\end{aligned} \tag{D1}$$

involve averaging of rank 5 tensor. This average is proportional to permutations of the following tensor:[30]

$$\delta_{\bullet\bullet}\epsilon_{\bullet\bullet\bullet}k_\eta, \qquad \bullet = \alpha, \beta, \gamma, \delta, \eta. \tag{D2}$$

We now examine the contribution of Eq. (D1) to $\mathcal{R}^{zx}_{xyzy}, \mathcal{R}^{zx}_{yxzy}, R^{zx}_{xyyz}, R^{zx}_{yxyz}$ tensor components. The wavevector of light k is parallel either with x or z axis, so the five indices in Eq. (D2) are formed by two pairs of same indices and one single index. Equation (D2) thus cannot contribute to $\mathcal{R}^{zx}_{[xy][yz]}$. The same argument also guarantees that $\mathcal{R}^{xx}_{[yz][yz]} = 0$.

APPENDIX E: $\sim(kR)^2$ TERMS IN THE HAMILTONIAN DO NOT CONTRIBUTE TO THE $\mathcal{R}^{zx}_{[xy][yz]}$ AND $\mathcal{R}^{xx}_{[yz][yz]}$ SIGNALS

The $\propto(kR)^2$ terms in field-matter Hamiltonian (Eq. (10)) describe electric octupole and magnetic quadrupole interactions,

$$H(\propto k^2) = E_\alpha k_\beta k_\gamma Y_{\alpha\beta\gamma}B^\dagger + h.c.$$

These contribute to the third-order response function to $\propto(kR)^2$ by

$$\begin{aligned}\mathcal{R}^{H(\propto k^2)}_{\alpha\beta\gamma\delta}(\propto (kR)^2) = k_{3,4;\phi}k_{3,4;\xi}\langle[\bar{Y}^*_{\alpha\phi\xi}(\tau_3)\bar{\mu}_\beta(\tau_2) + \bar{\mu}^*_\alpha(\tau_3)\bar{Y}_{\beta\phi\xi}(\tau_2)]\bar{\mu}_\gamma(\tau_1)\bar{\mu}^*_\delta(0)\rangle \\ + k_{1,2;\xi}k_{1,2;\phi}\langle\bar{\mu}^*_\alpha(\tau_3)\bar{\mu}_\gamma(\tau_2)[\bar{Y}_{\beta\phi\xi}(\tau_1)\bar{\mu}^*_\delta(0) + \bar{\mu}_\gamma(\tau_1)\bar{Y}^*_{\delta\phi\xi}(0)]\rangle.\end{aligned} \tag{E1}$$

We first prove that Eq. (E1) does not contribute in xz pulse setup to the relevant tensor components of $\mathcal{R}_c$.

$$\begin{aligned}\mathcal{R}^{zx;H(\propto(kR)^2)}_{\alpha\beta\gamma\delta}(\propto k^2) \\ = k^2\langle[\bar{Y}^*_{\alpha zz}(\tau_3)\bar{\mu}_\beta(\tau_2) + \bar{\mu}^*_\alpha(\tau_3)\bar{Y}_{\beta zz}(\tau_2)]\bar{\mu}_\gamma(\tau_1)\bar{\mu}^*_\delta(0)\rangle \\ + k^2\langle\bar{\mu}^*_\alpha(\tau_3)\bar{\mu}_\beta(\tau_2)[\bar{Y}_{\gamma xx}(\tau_1)\bar{\mu}^*_\delta(0) + \bar{\mu}_\gamma(\tau_1)\bar{Y}^*_{\delta xx}(0)]\rangle.\end{aligned} \tag{E2}$$

For $\mathcal{R}_{xyzy}, \mathcal{R}_{yxzy}, \mathcal{R}_{xyyz}$, and $\mathcal{R}_{yxyz}$ components, the nonvanishing isotropic rank 6 tensor must have paired indices,[30] but this is impossible if $\alpha, \beta, \gamma, \delta$ are some permutations of x, y, z, y, respectively. Thus,

$$\mathcal{R}^{zx;H(\propto(kR)^2)}_{[xy][yz]}(\propto k^2) = 0.$$

We turn to the xx pulse setup. In the slow φ limit,

$$\begin{aligned}\mathcal{R}^{xx;H(\propto k^2)}_{[yz][yz]}(\propto k^2) = -4k^2\langle\{[\mathrm{Im}[\bar{Y}^*_{yxx}(\tau_2)\bar{\mu}_z(\tau_2)] \\ + [\mathrm{Im}[\bar{\mu}^*_y(\tau_2)\bar{Y}_{zxx}(\tau_2)]\}[\mathrm{Im}[\bar{\mu}_y(0)\bar{\mu}^*_z(0)]]\rangle \\ - 4k^2\langle[\mathrm{Im}[\bar{\mu}^*_y(\tau_2)\bar{\mu}_z(\tau_2)] \\ \times\{[\mathrm{Im}[\bar{Y}_{yxx}(0)\bar{\mu}^*_z(0)] \\ + [\mathrm{Im}[\bar{\mu}_y(0)\bar{Y}^*_{zxx}(0)]]\}\rangle.\end{aligned} \tag{E3}$$

Since the dipole moment $\mu_+(\tau)$ is real and we find that the signal $\mathcal{R}^{xx;H(\propto k^2)}_{[yz][yz]}(\propto (kR)^2)$ (Eq. (E3)) vanishes for the symmetric exciton state. The same holds also for the antisymmetric state, but this requires more elaborate reasoning.

APPENDIX F: THIRD-ORDER RESPONSE OF THE ANTISYMMETRIC EXCITON

Third-order response is related to three components of isotropic rank 4 tensor,[30]

$$\begin{aligned}\mathcal{R}_{\alpha\beta\gamma\delta}(\propto (kR)^0) \\ = \frac{1}{30}\left[\delta_{\alpha\beta}\delta_{\gamma\delta}\tilde{\mathcal{R}}^{(1)} + \delta_{\alpha\gamma}\delta_{\beta\delta}\tilde{\mathcal{R}}^{(2)} + \delta_{\alpha\delta}\delta_{\gamma\beta}\tilde{\mathcal{R}}^{(3)}\right],\end{aligned} \tag{F1}$$

where

$$\begin{aligned}\tilde{\mathcal{R}}^{(1)} = 4\langle\mathcal{J}^*_\xi(\tau_3)\mathcal{J}_\xi(\tau_2)\mathcal{J}_\zeta(\tau_1)\mathcal{J}^*_\zeta(0)\rangle_\varphi \\ - \langle\mathcal{J}^*_\xi(\tau_3)\mathcal{J}_\zeta(\tau_2)\mathcal{J}_\xi(\tau_1)\mathcal{J}^*_\zeta(0)\rangle_\varphi \\ - \langle\mathcal{J}^*_\xi(\tau_3)\mathcal{J}_\zeta(\tau_2)\mathcal{J}_\zeta(\tau_1)\mathcal{J}^*_\xi(0)\rangle_\varphi,\end{aligned}$$

$$\begin{aligned}\tilde{\mathcal{R}}^{(2)} = 4\langle\mathcal{J}^*_\xi(\tau_3)\mathcal{J}_\zeta(\tau_2)\mathcal{J}_\xi(\tau_1)\mathcal{J}^*_\zeta(0)\rangle_\varphi \\ - \langle\mathcal{J}^*_\xi(\tau_3)\mathcal{J}_\xi(\tau_2)\mathcal{J}_\zeta(\tau_1)\mathcal{J}^*_\zeta(0)\rangle_\varphi \\ - \langle\mathcal{J}^*_\xi(\tau_3)\mathcal{J}_\zeta(\tau_2)\mathcal{J}_\zeta(\tau_1)\mathcal{J}^*_\xi(0)\rangle_\varphi,\end{aligned}$$

$$\begin{aligned}\tilde{\mathcal{R}}^{(3)} = 4\langle\mathcal{J}^*_\xi(\tau_3)\mathcal{J}_\zeta(\tau_2)\mathcal{J}_\zeta(\tau_1)\mathcal{J}^*_\xi(0)\rangle_\varphi \\ - \langle\mathcal{J}^*_\xi(\tau_3)\mathcal{J}_\xi(\tau_2)\mathcal{J}_\zeta(\tau_1)\mathcal{J}^*_\zeta(0)\rangle_\varphi \\ - \langle\mathcal{J}^*_\xi(\tau_3)\mathcal{J}_\zeta(\tau_2)\mathcal{J}_\xi(\tau_1)\mathcal{J}^*_\zeta(0)\rangle_{\varphi.}\end{aligned}$$

These relations are general and can be also used to derive Eq. (22).

In this Appendix we present calculation of 2D spectrum around the transition frequency of the $B^\dagger_-$ exciton. In the slow

φ limit, the $\propto(kR)^0$ signals (Eq. (F1)) are given by

$$\begin{aligned}\tilde{\mathcal{R}}^{(1)} &= 8|\tilde{\mu}_x|^4\langle 1\rangle_\varphi + 8\tilde{\mu}_z^4\langle \sin^2\varphi(\tau_2)\sin^2\varphi(0)\rangle_\varphi \\ &\quad + 16|\tilde{\mu}_x|^2\tilde{\mu}_z^2[\langle \sin^2\varphi(\tau_2)\rangle_\varphi + \langle \sin^2\varphi(0)\rangle_\varphi] \\ &\quad - 8\tilde{\mu}_z^2\big(|\tilde{\mu}_x|^2 + \mathrm{Re}\tilde{\mu}_x^2\big)\langle \sin\varphi(\tau_2)\sin\varphi(0)\rangle_\varphi, \\ \tilde{\mathcal{R}}^{(2)} &= 8|\tilde{\mu}_x|^4\langle 1\rangle_\varphi + 8\tilde{\mu}_z^4\langle \sin^2\varphi(\tau_2)\sin^2\varphi(0)\rangle_\varphi \\ &\quad + 4\tilde{\mu}_z^2|\tilde{\mu}_x|^2[-\langle \sin^2\varphi(\tau_2)\rangle_\varphi - \langle \sin^2\varphi(0)\rangle_\varphi] \\ &\quad + \tilde{\mu}_z^2\big(32|\tilde{\mu}_x|^2 - 8\mathrm{Re}\tilde{\mu}_x^2\big)\langle \sin\varphi(\tau_2)\sin\varphi(0)\rangle_\varphi, \\ \tilde{\mathcal{R}}^{(3)} &= 8|\tilde{\mu}_x|^4\langle 1\rangle_\varphi + 8\tilde{\mu}_z^4\langle \sin^2\varphi(\tau_2)\sin^2\varphi(0)\rangle_\varphi \\ &\quad + 4\tilde{\mu}_z^2|\tilde{\mu}_x|^2[-\langle \sin^2\varphi(\tau_2)\rangle_\varphi - \langle \sin^2\varphi(0)\rangle_\varphi] \\ &\quad + \tilde{\mu}_z^2(32\mathrm{Re}\tilde{\mu}_x^2 - 8|\tilde{\mu}_x|^2)\langle \sin\varphi(\tau_2)\sin\varphi(0)\rangle_\varphi. \end{aligned} \tag{F2}$$

By combining these signals we get Eq. (31).

We next investigate implications for signal $\mathcal{R}_c$ (Eq. (18)) from antisymmetric level. First, we look into the signal $\mathcal{R}^{zx}_{[xy][yz]}$ in xz pulse setup from antisymmetric exciton. Contributions $\propto(kR)^0$, $(kR)^1$ vanish and the leading $\propto(kR)^2$ contribution,

$$\begin{aligned}\mathcal{R}^{zx}_{[xy][yz]} \approx \frac{2(kR)^2}{15}\big\{&2\tilde{\mu}_z^4\langle\cos\varphi(t_2)\sin\varphi(t_2)\cos\varphi(0)\sin\varphi(0)\rangle_\varphi \\ &- |\tilde{\mu}_x|^2\tilde{\mu}_z^2\langle\cos\varphi(t_2)\cos\varphi(0)\rangle_\varphi\big\}.\end{aligned}$$

is identical to signal from symmetric level (Eq. (27)) and do not carry any additional knowledge.

It can be also proved $\tilde{\mathcal{R}}^{(2)} = \tilde{\mathcal{R}}^{(3)}$ for slow φ and real μ_x, so that mixed signal $\mathcal{R}_{[yz][yz]}$ has leading contribution $\propto(kR)^2$. However, since relation $\tilde{\mathcal{R}}^{(2)} \neq \tilde{\mathcal{R}}^{(3)}$ beyond these limits measurement of $\mathcal{R}^{xx}_{[yz][yz]}$ is of less valuable at the frequency of antisymmetric state, than at the symmetric state where $(kR)^0$ signal vanishes identically. Within this limit we again recover signal from the symmetric level (Eq. (28)) and consequently Eq. (29). Such a result seems less interesting, but it provides good reason to measure $\mathcal{R}_c$ when spectrum of symmetric and antisymmetric exciton overlap.

We have further analyzed nonlinear signals at the cross peaks between the symmetric and antisymmetric levels, we have not found useful information on the chirality dynamics therein.

APPENDIX G: THE PEAK VOLUME

We analyze the peak volume for the two chiral signals of the main text. Equation (30) is reduced to

$$\mathcal{R}_C(t_2) = \frac{k^2}{3}R^2|\tilde{\mu}_z|^4\int \mathcal{P}(\varphi,\varphi',t_2)\sin 2\varphi'\sin 2\varphi d\varphi d\varphi'. \tag{G1}$$

The integration in Eq. (G1) can be carried out analytically for the models of Appendix A. For model (i) (Eq. (A5)),

$$\mathcal{R}_C(t_2) = \frac{k^2}{3}R^2|\tilde{\mu}_z|^4 e^{-4\sigma^2}\sinh(4\sigma^2 e^{-Dt_2}), \tag{G2}$$

for model (ii) (Eq. (A7)),

$$\mathcal{R}_C(t_2) = \frac{4k^2}{3}R^2|\tilde{\mu}_z|^4\cos\varphi_0^2\sin^2\varphi_0 e^{-2\Lambda t_2}, \tag{G3}$$

and for model (iii) (Eq. (A8)),

$$\begin{aligned}\mathcal{R}_C(t_2) = \frac{k^2}{3}R^2|\tilde{\mu}_z|^4 e^{-4\sigma^2}e^{-\Lambda t_2} &\\ \times[\cos^2 2\varphi_0\sinh(4\sigma^2 e^{-Dt_2}) &\\ + \sin^2 2\varphi_0\{\cosh(4\sigma^2 e^{-Dt_2}) + e^{-\Lambda t_2} - 1\}].&\end{aligned} \tag{G4}$$

Equations (G2)–(G4) were employed to plot Fig. 8.

Similarly Eq. (32) for the signal $\mathcal{R}_D(t_2) \equiv \mathcal{R}_d(0,t_2,0)$ reduces to relation,

$$\mathcal{R}_D(t_2) = \frac{1}{6}|\tilde{\mu}_x|^2\tilde{\mu}_z^2\int \mathcal{P}(\varphi,\varphi',t_2)(\sin\varphi - \sin\varphi')^2\, d\varphi d\varphi',$$

which can be carried our analytically for model (i),

$$\mathcal{R}_D(t_2) = \frac{1}{3}|\tilde{\mu}_x|^2\tilde{\mu}_z^2 e^{-\sigma^2}[\sinh(\sigma^2) - \sinh(\sigma^2 e^{-Dt_2})], \tag{G5}$$

model (ii)

$$\mathcal{R}_D(t_2) = \frac{1}{3}|\tilde{\mu}_x|^2\tilde{\mu}_z^2\sin^2\varphi_0(1 - e^{-2\Lambda t_2}), \tag{G6}$$

and model (iii)

$$\begin{aligned}\mathcal{R}_D(t_2) = \frac{1}{3}|\tilde{\mu}_x|^2\tilde{\mu}_z^2 e^{-\sigma^2} &\\ \times\{\cos^2\varphi_0[\sinh(\sigma^2) - e^{-\Lambda t_2}\sinh(\sigma^2 e^{-Dt_2})] &\\ + \sin^2\varphi_0[e^{-\Lambda t_2}\cosh(\sigma^2) &\\ - e^{-\Lambda t_2}\cosh(\sigma^2 e^{-Dt_2}) &\\ + (1 - e^{-\Lambda t_2})^2\sinh^2(\sigma^2/2) &\\ + (1 - e^{-2\Lambda t_2})\cosh^2(\sigma^2/2)]\}.&\end{aligned} \tag{G7}$$

Equations (G5)–(G7) were employed to plot Fig. 9.

[1] E. Flapan, *When Topology Meets Chemistry: A Topological Look at Molecular Chirality* (Cambridge University Press, Cambridge, England, 2000).
[2] S. F. Mason, *Molecular Optical Activity and the Chiral Discriminations* (Cambridge University Press, Cambridge, England, 2009).
[3] *The Physical Chemistry of Chirality*, edited by J. M. Hicks (American Chemical Society, Washington, D.C., 2001).
[4] P. Mukhopadhyay, P. Wipf, and D. N. Beratan, Acc. Chem. Res. **42**, 809 (2009).
[5] M. Quack, J. Stohner, and M. Willeke, Annu. Rev. Phys. Chem. **59**, 741 (2008).
[6] *Circular Dichroism. Principles and Applications*, edited by N. Berova, K. Nakanishi, and R. W. Woody (Wiley, New York, 2000).
[7] L. Barron, *Molecular Light Scattering and Optical Activity* (Cambridge University Press, Cambridge, England, 2004).
[8] L. A. Nafie, T. A. Keiderling, and P. J. Stephens, J. Am. Chem. Soc. **98**, 2715 (1976).
[9] J. Kapitan, V. Baumruk, and P. Bour, J. Am. Chem. Soc. **128**, 2438 (2006).
[10] J. M. Hawkins, A. Meyer, and M. Nambu, J. Am. Chem. Soc. **115**, 9844 (1993).
[11] J. M. Hawkins and A. Meyer, Science **260**, 1918 (1993).
[12] S. F. Mason and B. J. Peart, J. Chem. Soc. Dalton Trans. **1977**, 937.
[13] C. Houssier and K. Sauer, J. Am. Chem. Soc. **92**, 779 (1970).
[14] D. M. Rogers and J. D. Hirst, Chirality **16**, 234 (2004).
[15] S. Brahms and J. Brahms, J. Mol. Biol. **138**, 149 (1980).
[16] G. Schütz, W. Wagner, W. Wilhelm, P. Kienle, R. Zeller, R. Frahm, and G. Materlik, Phys. Rev. Lett. **58**, 737 (1987).
[17] B. T. Thole, P. Carra, F. Sette, and G. van der Laan, Phys. Rev. Lett. **68**, 1943 (1992).

[18]J. H. Choi, S. Cheon, H. Lee, and M. Cho, Phys. Chem. Chem. Phys. **10**, 3839 (2008).
[19]M. Cho, *Two-dimensional Optical Spectroscopy* (CRC Press, Boca Raton, 2009).
[20]F. Hache, J. Photochem. Photobiol., A **204**, 137 (2009).
[21]P. Hamm and M. Zanni, *Concepts and Methods of 2D Infrared Spectroscopy* (Cambridge University Press, Cambridge, England, 2011).
[22]D. Abramavicius, B. Palmieri, D. V. Voronine, F. Šanda, and S. Mukamel, Chem. Rev. **109**, 2350 (2009).
[23]D. V. Voronine, D. Abramavicius, and S. Mukamel, J. Chem. Phys. **125**, 224504 (2006).
[24]T. Brixner and G. Gerber, Opt. Lett. **26**, 557 (2001).
[25]Y. Tang and A. E. Cohen, Phys. Rev. Lett. **104**, 163901 (2010).
[26]Y. Tang and A. E. Cohen, Science **332**, 333 (2011).
[27]F. Šanda and S. Mukamel, J. Chem. Phys. **124**, 124103 (2006).
[28]R. K. Kondru, P. Wipf, and D. N. Beratan, Science **282**, 2247 (1998).
[29]O. J. G. Somsen, R. van Grondelle, and H. van Amerogen, Biophys. J. **71**, 1934 (1996).
[30]D. L. Andrews and T. Thirunamachandran, J. Chem. Phys. **67**, 5026 (1977).
[31]E. Fick and G. Sauermann, *The Quantum Statistics of Dynamic Processes* (Springer-Verlag, Berlin, 1990).
[32]S. Mukamel, *Principles of Nonlinear Optical Spectroscopy* (Oxford University Press, New York, 1995).
[33]D. Gamliel and H. Levanon, *Stochastic Processes in Magnetic Resonance* (World Scientific, Singapore, 1995).
[34]Y. Tanimura, J. Phys. Soc. Jpn. **75**, 082001 (2006).
[35]N. A. Cherepkov, Chem. Phys. Lett. **87**, 344 (1982).
[36]R. L. Dubs, S. N. Dixit, and V. McKoy, Phys. Rev. Lett. **54**, 1249 (1985).
[37]D. Dowek, J. F. Pérez-Torres, Y. J. Picard, P. Billaud, C. Elkharrat, J. C. Houver, J. L. Sanz-Vicario, and F. Martin, Phys. Rev. Lett. **104**, 233003 (2010).
[38]K. Okomura, A. Tokmakoff, and Y. Tanimura, Chem. Phys. Lett. **314**, 488 (1999).
[39]C. Scheurer and S. Mukamel, J. Chem. Phys. **115**, 4989 (2001).
[40]M. Khalil, N. Demirdöven, and A. Tokmakoff, Phys. Rev. Let **90**, 047401 (2003).
[41]V. Szöcz, T. Palszegi, V. Lukeš, J. Sperling, F. Milota, W. Jakubetz, and H. F. Kauffmann, J. Chem. Phys. **124**, 124511 (2006).
[42]F. Šanda and S. Mukamel, J. Phys. Chem. B **112**, 14212 (2008).
[43]N. G. van Kampen, *Stochastic Processes in Physics and Chemistry* (North Holland, Amsterdam, 1992).
[44]G. E. Uhlenbeck and L. S. Ornstein, Phys. Rev. **36**, 823 (1930).
[45]H. Risken, *The Fokker-Plank Equation* (Springer-Verlag, Berlin, 1989).
[46]R. Kubo, "A stochastic theory of line shape and relaxation," in *Flucutation, Relaxation and Resonance in Magnetic Systems*, edited by D. ter Haar (Oliver and Boyd, Edingburgh, 1962), p. 23.
[47]P. W. Anderson, J. Phys. Soc. Jpn. **9**, 316 (1954).
[48]F. Šanda and S. Mukamel, J. Chem. Phys. **125**, 014507 (2006).
[49]F. Šanda, V. Perlík, and S. Mukamel, J. Chem. Phys. **133**, 014102 (2010).